Word Count: 13062, Revision 2

Evolution of layering in a migmatite sample: implications for the petrogenesis of multidomain monazite and zircon

Kaitlyn A. Suarez[1], Michael L. Williams[1], Timothy W. Grover[2], Michael J. Jercinovic[1], Claire R. Pless[3]

[1]Department of Geosciences, University of Massachusetts, Amherst, Massachusetts 01003, U.S.A. [2] Department of Earth and Atmospheric Sciences, University of Northern Colorado, Greeley, Colorado 80639, U.S.A. [3] Geology and Geography Department, Mount Holyoke College, South Hadley, MA 01075

Abstract

The timing of partial melting in high-grade metamorphic rocks is critical for constraining tectonic histories and processes. However, uncertainties exist about the behavior of monazite and zircon during partial melting, especially about the timing of crystallization with respect to melting reactions. This study is focused on a single sample (16TG143) of finely layered, migmatitic gneiss from the Adirondack Highlands, NY, interpreted to have undergone extensive biotite dehydration melting (i.e., Bt + Pl + Als + Qz = Grt + Kfs + melt). The rock contains one distinct leucosome layer. The non-leucosome (gray gneiss) portion of the migmatite has mm-scale sublayers with distinct differences in modes and mineralogy. The layers are interpreted to reflect the differential preservation of reactants and products formed during the forward and reverse progress of the melting reaction. Monazite and zircon modes, and to some degree, texture, composition, and geochronology all vary from layer to layer. Both minerals have up to three domains: ca. 1150 Ma anhedral cores, ca. 1050 Ma monazite mantles/fir tree textured

zircon, and ca. 1030 Ma rims. The heterogeneous layered gray gneiss provides robust constraints on the timing of melting (ca. 1050 Ottawan orogenesis), melt crystallization, and post-melting retrogression, in addition to information about earlier metamorphic events. Early-formed monazite and zircon grains were largely dissolved during progressive melting, except where preserved as relicts or inclusions. Monazite mantles and fir tree zircon grains precipitated upon cooling during progressive melt crystallization between temperatures of 800 to 750 ºC. Rims are interpreted to have precipitated during subsolidus, solid-state retrogression after ca. 1050 Ma. Correlations between the gneissic layering, melting reactions, and the character of geochronometers emphasize the importance of characterizing the layer-forming and chronometer petrogenesis processes as a critical part of deconvoluting the history of migmatitic gneisses.

Keywords: Petrochronology, migmatite, polymetamorphism, Adirondack Highlands, Monazite, Zircon, Gneiss

Introduction

Partial melting of high-grade metamorphic rocks has been observed in orogenic belts around the world (Korhonen et al. 2014; Kelsey and Hand 2015). The timing of partial melting has important implications for crustal rheology, the petrogenesis of igneous rocks, and interpretations of the regional tectono-metamorphic history. Traditionally, age constraints on partial melting have been obtained with U-Pb geochronology of zircon ($ZrSiO_4$), due to the refractory nature of zircon during high-temperature deformation and metamorphism. Recently, monazite has grown in popularity as a monitor of partial melting because advancements in in-situ microanalysis allow coupling of geochronologic data and trace element composition

(petrochronology) at high spatial resolution (Kylander-Clark et al. 2013; Kohn 2017; Williams et al. 2017).

Despite the ability to precisely measure U, Th, and Pb, the significance of monazite and zircon dates in partially melted rocks can be difficult to determine. Zircon and monazite have been interpreted to precipitate and grow during retrograde cooling and melt crystallization based upon theoretical modeling and experimental studies that suggest that monazite and zircon are soluble in many melt compositions (Kelsey et al. 2008; Spear and Pyle 2010; Yakymchuk and Brown 2014; Kohn et al. 2015; Yakymchuk 2017). However, several workers have suggested that zircon and/or monazite generations grew during partial melting events (Hermann and Rubatto 2003; Dumond et al. 2015; Hacker et al. 2015; Johnson et al. 2015; Blereau et al. 2016; Williams et al. 2019). If so, the age of these grains would constrain the timing of melting rather than melt crystallization. The question of monazite and zircon petrogenesis becomes even more important when analyzing orogenic belts that have experienced more than one phase of melting, because evidence of the first phase may be lost during subsequent dissolution/re-crystallization events (Williams et al. 2019).

The Adirondack Mountains of New York consist of uplifted Precambrian basement of the North American Grenville Province with extensive exposures of migmatitic rocks (Rivers 1997; Bickford et al. 2008; Chiarenzelli et al. 2017). Previous studies have constrained the timing of the Mesoproterozic tectonism, and it is generally accepted that two main events were associated with partial melting and garnet growth: 1) the Shawinigan Orogeny and associated magmatism (ca. 1190-1140 Ma) and 2) the Ottawan Orogeny (ca. 1080 – 1020 Ma) and associated unroofing and tectonic collapse (Rivers 1997; Bickford et al. 2008; McLelland and Selleck 2011; Wong et al. 2012; Regan et al. 2019; Williams et al. 2019). Metapelitic migmatitic paragneiss outcrops are

present along highway Rt. 4/22[1] south of Whitehall, NY. Monazite and zircon are interpreted to have grown during both the Shawinigan and Ottawan orogenies at this locality (Wong et al. 2012; Pless 2020), thus making this a suitable location to investigate geochronometer growth and preservation through multiple melting events.

The present study is focused on a single sample of finely layered migmatite. Our results indicate that the layers in the migmatite sample represent segregated products of the biotite dehydration melting reaction. Textures of monazite and zircon, and to some degree composition and geochronology, vary from layer to layer in the migmatitic rocks. Pre-, syn-, and post-melting monazite and zircon domains are preserved, but to differing degrees in the different layer types. Leucosomes, which at first would seem to best constrain the timing of melting, ultimately yield the most enigmatic results. Perhaps more than anything, our results emphasize the need for in-situ petrochronology using all layers of a migmatite to document the complete record of events.

Background

The Grenville Province of eastern North America (Fig. 1) is the product of a protracted period of Mesoproterozoic orogenesis and accretion that culminated in the formation of the supercontinent Rodinia (Rivers 1997; Chiarenzelli et al. 2017). The Adirondack Mountains are a domical uplift of Grenville Province rocks located in northern New York State. The uplift has been subdivided into two main domains, the Adirondack Lowlands (northwest) and Adirondack Highlands (southeast), separated by the Carthage-Colton mylonite zone (Fig. 1) (Mezger et al. 1992). The Adirondack Highlands, the focus of this study, are dominated by metaigneous (intrusive) rocks, although a variety of metasedimentary rocks are also present (Rivers 1997;

[1]The highway is officially designated as Rt. 4 and Rt. 22. For the purposes of this discussion, we will refer to it as Rt. 22.

Chiarenzelli et al. 2017; Williams et al. 2019). Intrusive rocks include tonalitic gneisses (ca. >1300 Ma), calc-alkaline gneisses (ca. 1185 Ma), anorthosite-mangerite-charnockite-granite (AMCG) (ca. 1160 Ma), gabbro/amphibolite (ca. 1160 Ma), and the Lyon Mountain Granite Gneiss (LMG) (ca. 1040 Ma) (McLelland et al. 2004) (Fig. 1). Metasedimentary rocks include garnet-rich migmatitic gneisses, interpreted to have been derived from Al-rich sedimentary protoliths (Storm and Spear 2005; Williams et al. 2019). Marble and calc-silicate rocks are also known to be present but are generally poorly exposed; their presence tends to be interpreted in low-lying areas with little or no bedrock exposure. The exposed metasedimentary rocks are dominated by garnet, sillimanite, quartz, feldspar, with variable amounts of prograde and retrograde biotite. Many of the metasedimentary rocks/localities have been described as "khondalite", a term originally used in the Eastern Ghats terrane of India for a sillimanite, quartz, garnet- rich rock with little to no biotite (Walker 1902; McLelland and Wong 2008).

The Precambrian rocks record a series of Mesoproterozoic accretionary/collisional orogenic events (Rivers 1997; McLelland et al. 2013; Chiarenzelli et al. 2017). The (ca. 1245–1225 Ma) Elzevirian orogeny is interpreted to represent a phase of arc magmatism and metamorphism related to the accretion of the Elzevir terrane (Rivers 1997). The (ca. 1190 – 1140 Ma) Shawinigan orogeny is interpreted to represent accretionary orogenesis, likely associated with the collision with a >1.3 Ga tonalitic arc (Rivers 1997; Heumann et al. 2006; Chiarenzelli et al. 2010; Wong et al. 2012). Voluminous emplacement of anorthosite-mangerite-charnockite-granite (AMCG) and gabbro occurred near the end of the Shawinigan orogeny (ca. 1155 Ma) and has been interpreted in terms of lithospheric delamination and underplating (McLelland et al. 2004; Regan et al. 2011). Emplacement of these magmas may have contributed to heating and melting in parts of the Adirondack Highlands (Chiarenzelli et al. 2010; Williams et al. 2019).

The (ca. 1090 – 1020 Ma) Ottawan orogeny is interpreted to represent a Himalayan-style continent-continent collision, possibly between Laurentia and Amazonia (Rivers 1997; Heumann et al. 2006; Bickford et al. 2008; Wong et al. 2012; Swanson-Hysell 2021). Subsequently, the Adirondack Highlands terrane was exhumed as a symmetrical gneiss dome or metamorphic core complex during the late-stage gravitational collapse of the Ottawan orogen (ca. 1060–1030) (Selleck et al. 2005; Wong et al. 2012; Regan et al. 2019; Rivers and Volkert 2023). Outcrops along Rt. 22 record down-to-the-east, normal shearing and fall within a domain defined as the eastern Adirondack shear zone, a broad and diffuse zone of non-coaxial strain interpreted to have accommodated extension during the late Ottawan orogeny (Wong et al. 2012). The last major regional event was the (ca. 1010- 980) Rigolet orogeny. This was a significant deformational event in the western Grenville Province, however, in the eastern Adirondack Mountains, this time period is mainly characterized by pegmatite and quartz vein emplacement and retrograde metamorphism (Valley et al. 2011; Williams et al. 2019).

Metasedimentary rocks of the Adirondack Highlands preserve evidence for multiple deformation events, although many rocks are dominated by a single intense fabric. Recently, Regan et al. 2015, distinguished four main fabrics/events in the Eagle Lake region of the northeastern Adirondacks. An older foliation (S1) is interpreted to have been folded and transposed by shallowly dipping F2 folds. The composite S1/S2 fabric was folded by open upright F3 folds, with axes plunging shallowly to the southwest. They are interpreted to have developed during the (ca. 1060 Ma) Ottawan extensional collapse. D4 is characterized by boudinage and late-stage (post Ottawan) pegmatite dikes (Regan et al. 2015). Additional structural analysis is needed to evaluate the degree to which this framework is applicable to the eastern Adirondack region in general.

This is the peer-reviewed, final accepted version for American Mineralogist, published by the Mineralogical Society of America.
The published version is subject to change. Cite as Authors (Year) Title. American Mineralogist, in press.
DOI: https://doi.org/10.2138/am-2022-8679. http://www.minsocam.org/

The metamorphic history and geochronology of the Adirondack Highlands have been constrained through petrographic analysis, petrologic modeling, thermobarometry, U-Pb zircon dating, and U-(Th)-Pb zircon and monazite U-Th-Pb_{total} geochronology (Spear and Markussen 1997; McLelland et al. 2004; Storm and Spear 2005; Heumann et al. 2006; Bickford et al. 2008; McLelland et al. 2013; Williams et al. 2019; Ferrero et al. 2021; Metzger et al. 2021). The Adirondack Highlands likely reached conditions above 800 °C and 7-9 kbar during the ca. 1050 Ma Ottawan orogeny (Spear and Markussen 1997; Storm and Spear 2005), and some workers have interpreted ultra-high temperature conditions (Ferrero et al. 2021; Metzger et al. 2021). Localities in the Adirondack Highlands are interpreted to have undergone melting during both the Shawinigan/AMCG and Ottawan events (Bickford et al. 2008; Williams et al. 2019). However, the extent of melting during the Shawinigan/AMCG event is unclear due to overprinted by the high to ultrahigh temperature Ottawan orogeny (Williams et al. 2019; Ferrero et al. 2021; Metzger et al. 2021). Further complicating this history, some localities in the Adirondack Highlands do not show evidence of Ottawan melting. We suspect that these localities were not fertile for subsequent melting due to exhaustion of either biotite or plagioclase during the first melting event (Heumann et al. 2006; Williams et al. 2019).

Methods

Field observations were made at a road cut along Rt. 22 south of Whitehall, NY (43.4658737°N, 73.4400611°W) (Fig. 1c). Results presented here come mainly from a single sample of layered migmatite (16TG143). Five polished thin sections were prepared that sampled the major compositional layers in the migmatite sample (Fig. 2). Two additional samples (17W001 and 17W002) were collected from distinct foliation-parallel leucosome layers in the

This is the peer-reviewed, final accepted version for American Mineralogist, published by the Mineralogical Society of America.
The published version is subject to change. Cite as Authors (Year) Title. American Mineralogist, in press.
DOI: https://doi.org/10.2138/am-2022-8679. http://www.minsocam.org/

outcrop (Fig. S1). All samples were cut parallel to the lineation and perpendicular to the gneissic layering/foliation. Samples corresponding to each of the polished sections were crushed for geochemical analysis at Bureau Veritas (Vancouver, British Columbia).

Polished thin sections were studied first by petrographic microscope and then by scanning electron microscope to document assemblages, textures, and microstructures in each compositional layer. These sections were subsequently analyzed with the Cameca SX100 and Cameca SX5 Tactis microprobes at the at the University of Massachusetts, Amherst. Entire thin sections were compositionally mapped for Mg *K*α, K *K*α, Ca *K*α, Si Kα, Al *K*α, Ti Kα, P *K*α, Ce *L*α, and Zr *L*α in order to: 1) observe the distribution of major silicate phases, 2) locate monazite and zircon grains, and 3) calculate modes of all major and minor phases (Fig. 3) (Williams et al. 2006; Williams et al. 2017). The full section compositional maps were stacked using Adobe Illustrator to locate monazite and zircon grains in the context of the major phases. Major silicate phases (e.g., garnet, plagioclase) were compositionally mapped for Mg, K, Ca, Si, Al, Ti, and Fe to guide quantitative compositional analysis with the electron microprobe.

Monazite U-Th-Pb$_{total}$ Petrochronology

Approximately 25 monazite grains from each polished thin section were mapped at high resolution for Y *L*α, Th *M*α, U *M*β, Ca *K*α, and Si *K*α to delineate compositional domains. The compositional grain maps were simultaneously processed such that image intensities are directly comparable from grain to grain within a single sample (see Williams et al. 2006, 2017). The monazite grain maps were then placed around the full-section map using Adobe Illustrator, with links to exact grain locations, to evaluate the monazite setting and to better interpret the textural and zoning significance (see Williams et al. 2006). Monazite domains were delineated based on

183 texture and composition. Each domain type was analyzed multiple times in each sample, with
184 priority given to analyzing multiple domains in the same grain.

185 U, Th, and Pb and a suite of 22 trace and rare earth elements were analyzed on the
186 Ultrachron electron microprobe at the University of Massachusetts Amherst (Table S1). The
187 Ultrachron electron microprobe was specifically designed for trace-element analysis and U-Th-
188 Pb_{total} geochronology (Jercinovic et al. 2008). Background measurements for U, Th, and Pb
189 employed a multipoint technique, which involves regressing multiple background measurements
190 above and below the peak position (Allaz et al. 2019). This is essential for accurate EPMA
191 dating; background analysis by two-point linear interpolation can result in > 100 ppm error in
192 trace element analyses due to curvature in the Bremsstrahlung spectrum and, especially,
193 background interferences (Jercinovic and Williams 2005). The Moacyr Brazilian pegmatite
194 monazite was used as an internal consistency standard ($^{207}Pb/^{235}U$ age of 506.7 ± 0.8 Ma (2σ,
195 MSWD = 0.83)) (Gasquet et al. 2010; Wong et al. 2012; Allaz et al. 2019). The Moacyr
196 reference monazite was run before, during, and after the analyses. The results generally yielded
197 dates within 2 or 3 m.y. of 506.7 Ma and well within 1%. When the Moacyr results fell
198 consistently outside the standard deviation, the instrument was recalibrated, and the analytical
199 session was rerun for standards and unknowns. Additional descriptions of the methods are
200 provided in the Supplementary Material.

201 Rare earth element analysis employed a shared background approach. Numerous
202 background measurements were made over a spectrometer range covering the REE peak
203 positions. Filtering and regression analysis was used to calculate the background curvature and
204 background intensity under each peak. Advantages of the shared background method include: 1)
205 accurate determination of background curvature, 2) elimination of background measurements

affected by interference or absorption, and 3) improvement of counting statistics on background measurements (see Allaz et al. 2019).

For this study a single "date" is defined as one high-resolution background analysis and six or more peak measurements made immediately adjacent to the background position (Williams et al. 2017). The date is calculated using the age equation of Montel (1996), and the uncertainty is calculated both by propagating peak and background errors through the age equation and by statistics on repeated peak measurements (Montel et al. 1996; Williams et al. 2006; Williams et al. 2019). Each date is plotted as a single Gaussian probability distribution function (Williams et al. 2019). Color codes show the main domain types (i.e., core, mantle, rim). Typical uncertainties (2σ) range from ca. 8 m.y. to ca. 20 m.y.. Uncertainties larger than 40 m.y. typically reflect compositional heterogeneity within the domain and were excluded in this study. Additional details about domain-specific dating, and trace element analysis are summarized in Williams et. al. (2006; 2017) and Dumond et al. (2008). All dates in the text are reported at the two sigma (2σ) confidence interval. Throughout the text we use the term "date" to refer to analytical results and reserve "age" for the interpretation of the dates (Schoene et al. 2013; Williams et al. 2019).

Zircon U-Pb Geochronology

Zircon grains were dated at the University of Arizona LaserChron laboratory using a Thermo Element-2 single-collector laser ablation inductively coupled plasma mass spectrometer (LA-ICPMS). Zircon separates were prepared at the University of Arizona. A single three-cm-thick leucosome layer (sample 16TG143-5) was separated from the rest of the migmatite sample

before crushing and separate preparation. Two zircon separates were analyzed: migmatite and leucosome.

Zircon grains were first separated from the rock and then grains were hand-picked and mounted in epoxy. Low-resolution cathodoluminescence (CL) and backscattered electron (BSE) imaging was used to characterize grains prior to dating. 300 spots from 170 grains were analyzed from the migmatite separate, and 40 spots from 35 grains were analyzed from the leucosome separate. Where possible, zircon core and rim domains were chosen for analysis with a laser spot size of 15 μm. Dated zircon grains were subsequently imaged with high resolution CL at the University of Massachusetts Amherst using a Zeiss EVO50 SEM with a Gatan Mini CL detector. Results were filtered and classified according to the location of analytical spots. Results with greater than 95% concordance were evaluated, and all other discordant grains were removed from the populations. The Sri Lanka ($^{206}Pb/^{238}U$ age of 563.5 ± 2.3 Ma), FC ($^{207}Pb/^{206}Pb$ age of 1099 ± 2 Ma), and R33 ($^{206}Pb/^{238}U$ age of 419.3 ± 0.4 Ma) zircon grains were used as internal consistency standards. The results from the zircon standards yielded dates within the individual standard deviations. See Gehrels et al. (2006, 2008) for the Laser Ablation ICP Mass Spectrometry methods at the Arizona LaserChron laboratory.

Thermobarometry

Thermobarometry was carried out using winTWQ version 2.32 (Berman 1991, 2007). The internally consistent thermodynamic database (DEC06.DAT) was utilized (see Berman 2007). The activity models used for garnet and biotite were taken from Berman et al. 2007 and the plagioclase activity model was taken from Fuhrman and Lindsley (1988). The winTWQ thermobarometer uncertainties are approximately ± 50 °C, ± 0.1 GPa. Zr-in-rutile thermometry

was calculated using the combined equation in Kohn (2020) where temperature uncertainties are ± 10-15 °C. Ti-in-biotite thermometry (Wu and Chen 2015) temperature uncertainties are reported to be ± 50 °C.

Results

Sample 16TG-143, the main focus of this work, was collected from an outcrop of metapelitic migmatite located approximately 10 km south of Whitehall, NY (Fig. 1,2). At this locality, gneissic layering is defined by leucosome layers and by subtle color variation in the gray-colored gneiss. A strong layer-parallel foliation is defined by sillimanite and biotite. The fabric has an NNE strike (~019°) and a shallow dip ~20° to the southeast. A relatively strong mineral lineation (plunging 16° toward 131°) is defined by sillimanite, quartz rods, and elongated biotite books. The shear sense is predominately top-to-the-southeast (normal) based on asymmetric tails on σ-type K-feldspar and garnet porphyroclasts (Wong et al. 2012).

Sample 16TG143 is a layered, garnet-rich, gray migmatitic gneiss with leucosome layers that are millimeters to centimeters in thickness. The non-leucosome layers contain lavender-colored garnet, biotite, K-feldspar, plagioclase, sillimanite, and quartz with accessory ilmenite, apatite, rutile, pyrite, monazite, and zircon. Leucosome layers contain K-feldspar, plagioclase, quartz with accessory garnet, biotite, apatite, pyrite, ilmenite, rutile**,** monazite, and zircon. Two relatively thick (~15 cm) leucosome layers were sampled from the same outcrop area and analyzed for comparison with the leucosome layers in sample 16TG143. The leucosome samples (17W001 and 17W002) are dominated by quartz, plagioclase, and K-feldspar. Garnet is distinctly less abundant in comparison to sample 16TG143. Accessory phases in the external leucosomes include sillimanite, biotite, apatite, pyrite, ilmenite, rutile**,** monazite, and zircon.

274

275 **Multiscale Compositional Layering**

276 The paragneiss rocks at the outcrop scale are dominated by the two basic layer (color)
277 types: gray gneiss and leucosome. However, on the thin section scale, and especially on
278 compositional maps, the gneiss can be subdivided into distinct sublayer types based primarily on
279 modes and textures of silicate minerals (Table 1). The thin-section-scale sublayers are typically
280 parallel to the gneissic fabric, but boundaries between layers can be gradational and irregular on
281 a fine scale. We distinguish four end-member layer types in sample 16TG143, and we divide
282 Type 1 layers into two subtypes (Fig. 4).

283 **Type 1a.** Type 1a layers consist of K-feldspar, plagioclase, quartz, garnet, biotite, and
284 sillimanite (Fig. 5a). Garnet is abundant, up to 25%; crystals are generally 1 to 5 mm in diameter
285 and distinctly anhedral. Typically, several (1-3) K-feldspar porphyroclasts (up to 3 mm in
286 diameter) are present in the layer and display a sigma-type geometry defined by dynamically
287 recrystallized core and mantle structures (White 1976). The matrix consists of equigranular,
288 largely annealed K-feldspar, plagioclase, quartz, with local fine biotite and sillimanite. Coarse
289 biotite and sillimanite form asymmetric tails, and locally, extend into and postdate the anhedral
290 garnet crystals (Fig. 5b). **Type 1b.** Type 1b layers also contain of K-feldspar, plagioclase, quartz,
291 garnet, biotite, and sillimanite. However, garnet is more abundant than in Type 1a layers, up to
292 35%. Like garnet in Type 1a, the crystals are generally 1 to 5 mm in diameter and distinctly
293 anhedral. In the matrix, K-feldspar and quartz are less abundant, and plagioclase, biotite, and
294 sillimanite are somewhat more abundant than in Type 1a layers. Like Type 1a layers, coarse-
295 grained biotite and sillimanite are distinctly associated with, and extend into garnet
296 porphyroblasts (Fig. 5a, b).

297 **Type 2.** Type 2 layers are dominated by K-feldspar and quartz (Fig. 5a). Large, lens-
298 shaped, dynamically recrystallized K-feldspar porphyroclasts (up to 7 mm in diameter) have a
299 sigma-type geometry defined by core and mantle structures. Recrystallized K-feldspar laminae
300 extend parallel to foliation. Narrow, quartz ribbons with sharp, parallel-sided boundaries also
301 extend parallel to foliation and are locally deflected around K-feldspar porphyroclasts. Based on
302 the extreme length, constant thickness, and sharp boundaries, the quartz ribbons are interpreted
303 to represent deformed veins. Plagioclase occurs primarily as exsolution lamellae in the K-
304 feldspar. Garnet (5%) is less abundant than in Type 1 layers, generally appearing as small (1-2

mm), euhedral crystals most commonly surrounded by K-feldspar (Fig. 5c). Biotite is absent except for fine inclusions in K-feldspar.

Type 3. Type 3 layers consist of plagioclase, quartz, and garnet (Fig. 5a). Recrystallized, equigranular plagioclase makes up 60% of the matrix. The grains have straight, clean 120° triple junctions (i.e., equilibrium textures). The quartz ribbons in Type 3 layers are thin, relatively short and have tapered boundaries; aspect ratios are approximately 5:1 or less. We interpret these wormy ribbons to represent deformed quartz grains, although some may be dismembered veins. The garnet crystals (15%) are 1 to 3 mm in diameter and unlike those in Type 1 layers, are distinctly euhedral (Fig. 5d). Minor biotite and sillimanite are dispersed throughout the layers but are not spatially associated with garnet.

Type 4. Sample 16TG143 contains one three-cm-thick leucosome layer, classified here as a Type 4 layer. Plagioclase porphyroclasts (up to 5 mm in diameter) display a sigma-type geometry defined by dynamically recrystallized core and mantle structures. K-feldspar occurs as lens- or rod- shaped domains of equigranular feldspar extending parallel to the gneissic layering. Wide, parallel-sided quartz ribbons extend parallel to the layering and are deflected around garnet and plagioclase porphyroclasts. Small (1-3 mm) subhedral to euhedral-shaped garnet (5%) are dispersed in the layer along with minor amounts of fine-grained biotite. Sericite is present in the matrix, and especially near the contacts with the gray gneiss.

External Leucosomes. Two relatively thick (~15 cm) leucosome layers (17W001 and 17W002) were collected and analyzed for comparison with the leucosome layer(s) in the primary sample. Plagioclase, K-feldspar, and quartz are the dominant phases. Intergrown K-feldspar and plagioclase extend parallel to the gneissic layering. Very large, parallel-sided quartz ribbons cross the layering and are deflected around garnet and feldspar porphyroclasts. Garnet (5%) is

328 less abundant than in the Type 4 layer and occurs as (3-5 mm diameter) subhedral to euhedral
329 crystals. Coarse-grained, lineation-parallel sillimanite is present as a minor phase. Biotite is rare.
330
331 **Mineral Compositions.** The compositions of most major phases are similar in all layer
332 types (Table S1). The major minerals show relatively little zoning. The average garnet
333 composition is Alm_{57}, Pyr_{37}, Grs_{04}, Sps_{01}. The average plagioclase composition is Ab_{68}, An_{31},
334 Ksp_{01}. K-feldspar is Ksp_{89}, Ab_{11}, An_{01}. There is, however, some variation in the biotite
335 composition. The average biotite Mg# (Mg/Mg+Fe) is 0.72 in Type 1a and 1b layers. The
336 average biotite Ti content is 5 wt% TiO_2. In contrast, the average Mg# is 0.65 in Type 2, 3, and 4
337 layers and in the external leucosomes, and the TiO_2 content is 5.5 wt%.
338
339 ***P-T* Conditions and Melting Reactions**
340 The primary assemblage in sample 16TG143 sample includes garnet, K-feldspar, quartz,
341 sillimanite, biotite, and plagioclase. Much of the biotite and sillimanite appear to be relatively
342 late, occurring around and extending into garnet. Based on the abundance of garnet and K-
343 feldspar, the lack of muscovite, and rarity of prograde/peak biotite, we suggest that melting
344 occurred via a biotite dehydration melting reaction, such as:
345 Bt + Pl + Als + Qz = Grt + Kfs + melt (1)
346
347 Bt + Als + Qz = Grt + Kfs + melt (2)
348 This interpretation is consistent with the granulite-facies conditions and with interpretations of
349 previous workers in the region (Spear and Markussen 1997; Storm and Spear 2005; Heumann et

al. 2006; Bickford et al. 2008; Williams et al. 2019). If muscovite was originally present in these Al-rich rocks, some earlier melting might have involved muscovite dehydration (see below).

We used several thermobarometers to estimate pressures and temperatures at this locality (Table 2). The Zr-in-rutile thermometer (Kohn 2020) suggests a temperature on the order of 800 ± 15 °C (~1550 ppm zirconium) as determined from grains in the Type 1 and 3 layers (see supplementary material). The Ti-in-biotite thermometer (Wu and Chen 2015) indicates a temperature of approximately 725 ± 50 °C for Type 2-4 layers and the external leucosomes. Type 1 layers yield approximately 700 ± 50 °C, which is consistent with the lower biotite Mg#. The garnet, aluminosilicate, quartz, plagioclase (GASP) barometer yields a pressure of approximately 0.8 ± 0.1 GPa at 800 ± 50 °C for a near rim garnet composition (Berman 2007). Spear and Markussen (1997) calculated a pressure on the order of 0.7 GPa for the eastern Adirondack Highlands.

Bulk Composition

The bulk composition of 16TG143 is reported in Table S2. As discussed below, we apply the pseudosection and theoretical models of Yakymchuk (2017) to sample 16TG143. Therefore, we normalized the composition of 16TG143 to assume a similar water content (6 wt%). We note that the starting bulk composition used for modeling in Yakymchuk (2017) is nearly identical to 16TG143; however, sample 16TG143 is slightly richer in aluminum.

Accessory/Chronometer Phases

The abundance of monazite and zircon differ significantly from layer to layer in the sample (Fig. 6a) (Table 3). Monazite and zircon are most abundant in Type 1 layers. Type 1a

layers have approximately 8 monazite and 10 zircon grains per cm^2; Type 1b layers have about 17 monazite and 23 zircon grains per cm^2. Type 2 layers contain relatively few accessory chronometers (2 monazite and 4 zircon grains per cm^2). Type 3 layers have approximately 6 monazite and 7 zircon grains per cm^2. The Type 4 (leucosome) layer contains about 4 monazite and 9 zircon grains per cm^2. Fewer grains occur in the external leucosomes, averaging 1 monazite and 1 zircon per cm^2.

The textures of monazite grains also differ among the layers. Monazite grains in Type 1 layers tend to have an irregular shape, with grain boundaries somewhat controlled by nearby minerals, commonly biotite or garnet (Fig. 6b). The grains vary from tens to hundreds of micrometers in diameter. Monazite grains in Type 2 layers have more euhedral shapes (Fig. 6c). The grains are consistently large, with diameters near 100 μm. Type 3 monazite grains tend to be small (20-50 μm) and equant in shape (Fig. 6d). Monazite in the Type 4 (leucosome) layer has abundant inclusions of fine U and Th-rich inclusions and apatite near and within the grain margins, interpreted to reflect (late?) alteration (Fig. 6e). The monazite grains range from ten to hundreds of micrometers in diameter. Monazite grains in the external leucosomes are small (~5-30 μm) and equant, with no apparent alteration (Fig. 6f).

Monazite Results, Type 1-3. We analyzed more than 100 monazite grains from the Type 1-3 layers**,** including grains present in the matrix and inclusions in garnet. Most grains have multiple compositional domains. Yttrium concentration most clearly defines the major subdomains, but Th, U, trace, and rare earth concentrations also vary between Y-defined domains. High-Y cores are present in approximately one-third of all monazite grains. The cores tend to be small, approximately 10-20 μm in diameter and anhedral to subhedral in shape. The cores are surrounded by a low-Y mantle, the largest domain in most monazite grains. Most

matrix monazite grains have narrow (ca. 5 μm wide) high-Y rims. Monazite inclusions in garnet commonly lack high-Y rims. In general, high-Y cores yielded dates around 1170-1150 Ma (n=13). The low-Y mantle domains yielded dates ranging from 1080-1040 Ma (n=60). High-Y rims generally yielded dates 1040-1000 Ma (n=29) (Fig. 7a)

Figure 7b is a plot of Y-content in monazite vs. date. Horizontal lines are 2σ uncertainties associated with the calculated date. These are shown here to give a sense of the magnitude of uncertainty but are omitted in subsequent figures (Fig. 8a); relative errors can be seen on the Gaussian distributions. Typical uncertainties are ca. 10 Ma; all uncertainties are provided in the supplement (Table S3). Figure 8b shows the sum of the heavy rare earth elements (HREEs) in monazite vs calculated date. The sum of the HREEs decrease from approximately 30,000 ppm in the cores to 10,000 ppm in the mantles, while Y decreases from approximately 15,000 to 1,000 ppm. Y and HREE content increase in monazite rims in all layers, however there are some slight differences. Type 1 and 3 layers have the highest Y and HREE rim content with dates ranging from ca. 1050 to 1000 Ma. Monazite rims in Type 2 layers have a much narrower range of dates (ca. 1050 Ma) and have lower Y and HREE compared to Type 1 and 3 layers.

The behavior of uranium, thorium, sulfur, and calcium show consistent trends across all layers. U decreases from about 4,000 ppm in the cores to 1,000 ppm in the mantles and then increases in the rims to approximately 6,000 ppm (Fig. 8c). The Th content (Fig. 8d) ranges between about 25,000 to 35,000 ppm in the cores and mantles. The rims range from 15,000 to 30,000 ppm. The sulfur and calcium content of monazite increase dramatically in the ca. 1050 mantle domains (Fig. 8e, f); this increase has been observed in other studies of biotite dehydration melting (Laurent et al. 2016) (see discussion below).

Traverses across the monazite mantles were collected to look for systematic compositional variations during melt crystallization. U content remains extremely low in the mantles (~1,000 ppm). However at high-resolution, U increases and decreases in cycles by about 200 ppm (Fig. 9).

Monazite inclusions in garnet are most abundant in layer Types 1 and 3, consistent with the greater abundance of garnet in these layers. The inclusions occur as small, equant grains (10-20 μm). Typically, each inclusion is dominated by a single compositional domain, either entirely high-Y or entirely low-Y, although several have a core and a mantle. The high-Y (core) domains in garnet are more abundant, larger, and more euhedral in shape compared to matrix monazite. The high-Y inclusions have approximately 16,500 ppm yttrium and yield ca. 1150 Ma dates, consistent with the composition and dates of the matrix cores. The low-Y inclusions have about 2,000 ppm yttrium and yield ca. 1050 Ma dates (Fig. 10).

Monazite Results, Type 4. We analyzed fifteen monazite grains in the Type 4 (leucosome) layer. Only one grain was included in garnet. The grains have a similar core-mantle-rim zonation as those in gneiss-hosted grains. The boundaries, however, are more irregular and the Y content in each domain is somewhat heterogeneous or patchy. High-Y cores are small (2-10 μm) and anhedral in shape. The grains are dominated by mantle domains (10-100 μm in width) with thin (2-5 μm) rims.

Monazite dates are generally consistent with those in Type 1-3 layers. High-Y cores yield ca. 1170-1150 Ma dates (n=10). The low-Y mantle domains yield dates ranging from 1070-1050 Ma (n=12). High-Y rims yield dates 1040-1030 Ma (n=6) (Fig. 11).

This is the peer-reviewed, final accepted version for American Mineralogist, published by the Mineralogical Society of America.
The published version is subject to change. Cite as Authors (Year) Title. American Mineralogist, in press.
DOI: https://doi.org/10.2138/am-2022-8679. http://www.minsocam.org/

Yttrium and HREEs follow the similar high-low-high pattern (Fig. 12a, b). Although depleted, the mantles are not nearly as depleted in Y or HREEs as the Type 1-3 monazite grains. Y decreases from approximately 20,000 ppm in the cores to 3,000 ppm in the mantles, while HREE decrease from approximately 30,000 to 17,000 ppm. In the rims, Y increases slightly to approximately 8,000 ppm and HREE increase to 22,000 ppm.

Uranium is more variable in Type 4 grains compared to Type 1-3 grains (Fig. 12c). U decreases from approximately 4,000 ppm in the cores to 2,500 ppm in the mantles and then increases slightly to 3,000 ppm in the rims. Thorium content is significantly greater compared to Type 1-3 grains (Fig. 12d). The Th content ranges between about 50,000 to 70,000 ppm in the cores and about 75,000 to 85,000 ppm in the mantles. The rims range from 70,000 to 80,000 ppm. Sulfur and calcium follow the similar low-high-low pattern (Fig. 12e, f).

Monazite Results, External Leucosomes. We analyzed sixteen monazite grains in external leucosome layers. Thirteen of the sixteen grains are essentially unzoned and can be divided into two compositional populations: high-Y and low-Y. The unzoned grains are approximately 20 to 50 μm in diameter. Two of the zoned grains display core-mantle-rim zonation while one displays a mantle and a rim. The cores are euhedral in shape and are approximately 15-25 μm in diameter.

Monazite from the external leucosomes yield distinct dates from monazite in sample 16TG143. No ca. 1150 Ma dates were obtained from any domains. The cores yielded 1066 and 1064 Ma ± 4 Ma dates. The mantles yielded 1066 ± 5 and 1042 ± 9 Ma dates. The rims yielded dates that range from 1050 to 1030 Ma (n=4). In the unzoned population, the high-Y grains

462 yielded dates ranging from 1050 to 1000 Ma (n=4). The low-Y grains yielded dates ranging from
463 1040 to 980 Ma (n=6) (Fig. 13).

464 Unlike the zoned grains in the Type 1-4 layers, the cores contain only slightly more Y
465 and HREEs than the mantle domains (Fig. 14a, b). Y decreases from approximately 6,000 ppm
466 in the cores to 4,000 ppm in the mantles, while HREE decreases from about 25,000 to 18,000
467 ppm. Y increases to approximately 12,000 ppm and HREE increases to 30,000 ppm in the rims.
468 High-Y, unzoned grains contain significantly more Y and HREEs, 25,000 ppm and 40,000 ppm,
469 respectively, than any of the domains in the zoned grains or the low-Y, unzoned grains.

470 Uranium content is noticeably higher in the external leucosome monazite compared to
471 grains in Type 1-4 (Fig. 14c). U decreases from approximately 22,000 ppm in the cores to 11,000
472 ppm in the mantles, and then increases slightly to approximately 12,000 ppm in the rims. The
473 average U content in the unzoned grains is 13,000 ppm. Th content in the zoned grains is
474 generally comparable to the grains in Type 4 layers (Fig. 14d), while Th content in the unzoned
475 grains is significantly lower, ca. 100-5000 ppm. S and Ca content in the zone and unzoned grains
476 are generally comparable to Layer 1-4 grains (Fig. 14e, f).

477

478 **Zircon Results.** Zircon grains were separated from a sample containing layer Types 1-3.
479 Although we did not separate the individual layer types, CL and BSE analysis of thin sections
480 shows that similar zircon textures are present in each of the three layer types. The grains are
481 round with diameters ranging from 20 to 100 μm. Some zircon grains exhibit cores (in BSE),
482 while others are homogeneous. Cores are dark in CL and display prismatic shapes with
483 oscillatory zoning. The cores are 20-40 μm in length with an aspect ratio of approximately 2:1.
484 Most grains display a distinct style of sector zoning texture known as “fir tree” sector zoning that

485 is characterized by sharply defined zigzag boundaries (Raven and Dickson 1989; Corfu et al.
486 2003; Rubatto 2017) (Fig. 15). Thin (~5 μm) rims are present around some of the grains.
487 Three hundred zircon spots were analyzed from 170 grains. Where possible, multiple
488 domains were analyzed in the same grain. The cores can be divided into two populations. Two
489 grains yielded $^{207}Pb/^{206}Pb$ dates of 1240 ± 16 and 1262 ± 17 Ma (2σ), while four grains yielded a
490 weighted mean of 1145 ± 20 Ma (MSWD= 1.66). The vast majority of zircon grains, with fir tree
491 textures, yielded a weighted mean $^{207}Pb/^{206}Pb$ date of 1045 ± 4 Ma (n=113; MSWD= 0.40) (Fig.
492 15) (Table S5). The rims were too thin to analyze.
493 Zircon was separated from the Type 4 (leucosome) layer. The grains are 100 to 300 μm
494 in length with an aspect ratio of approximately 2:1. The grains exhibit oscillatory zoning in BSE.
495 In CL, dark, oscillatory zoned cores are surrounded by narrow (2-20 μm), CL-bright, rims (Fig.
496 16). No grains exhibit fir tree sector zoning. Twelve zircon cores yielded a weighted mean of
497 1163 ± 12 Ma (2σ, MSWD= 1.15). Only two rims were thick enough for analysis and both
498 yielded dates of 1050 Ma, with 2σ errors of 18 and 20 Ma (Fig. 16) (Table S4). We were unable
499 to date the external leucosome layers as no zircon was recovered from the separation process.
500

501 **Discussion**

502 **Petrogenesis of Gneissic Layering**

503 The gray (non-leucosome) part of sample 16TG143 can be divided into distinct layer
504 types based on modes and textures of silicate minerals. Because the abundance and character of
505 monazite and zircon vary between layer types, interpretations of the U(Th)-Pb dates depend to
506 some degree on interpretations of the layers themselves. As discussed below, the layer types can
507 be interpreted in the context of the reactants vs. products of the interpreted biotite dehydration

508 melting reactions (Eq 1, 2). In the following sections we first discuss the petrogenesis of the
509 layer types and then evaluate and interpret the zoning and dating of the chronometer phases.
510 Biotite and sillimanite are most abundant in the Type 1 layers, specifically Type 1b
511 layers. We suggest that these "reactant" phases, to a large extent, grew through a reversal of the
512 melting reaction as supported by the anhedral, remnant (i.e., unstable) garnet with crosscutting
513 (late) biotite and sillimanite, and by abundant matrix plagioclase and quartz (Fig 5b). The
514 reversal is interpreted to occur while melt is progressively crystallizing, but not yet fully
515 crystalline. Type 1b layers may reflect a more significant degree of reversal of the melting
516 reaction, as interpreted by the rarity of K-feldspar and the greater abundance of biotite and
517 sillimanite. During cooling, a sufficient amount of the melt (+H_2O) was apparently retained in
518 the layer, and not significantly segregated, for the reversal of the reaction.
519 Type 2 layers contain only rare reactant phases (bt, plag, sill) and instead are dominated
520 by K-feldspar and euhedral garnet (Fig. 5c). That is, Type 2 layers primarily contain the solid
521 products of the melting reaction. We hypothesize that any melt (+H_2O) present in the layer was
522 largely removed, which inhibited retrogression in this layer.
523 Type 3 layers contain distinctly euhedral garnet, abundant plagioclase, and quartz with
524 little or no late biotite or sillimanite (Fig. 5d). We suggest that these layers contain some amount
525 of crystallized melt in addition to the solid products of the melting reaction and the remaining
526 reactants. We were not able to distinguish multiple garnet populations/generations, but it is
527 possible that some garnet may have crystallized as phenocrysts based on the euhedral shapes
528 (Taylor and Stevens 2010; Dorais and Tubrett 2012) The lack of late biotite and sillimanite
529 suggests little retrogression. It is notable that K-feldspar, the other solid product of the melting

530 reaction, is relatively rare in the Type 3 layers. We suspect that the K-feldspar crystallized in
531 separate Type 2 layers rather than within the melt-rich Type 3 layers.

532 The compositions of the major silicate minerals are generally consistent across all layer
533 types. We take this to suggest that the minerals were produced during a single melting event or
534 that the minerals equilibrated under high-temperature conditions. There are, however, distinct
535 differences in the composition of biotite. The Mg# for biotite in the Type 1 layers is noticeably
536 higher at 0.72 than an average of 0.65 for all other layer types. In general, with similar garnet
537 compositions a higher biotite Mg# would represent a lower crystallization temperature (Ferry
538 and Spear 1978), consistent with our interpretation of retrograde biotite in Type 1 layers. As
539 noted, biotite in Type 1 layers records Ti-temperatures of ~700 °C while biotite in the other
540 layers record ~725 °C (Wu and Chen 2015).

541 In summary, our observations suggest that the gneissic layering in the 16TG143 sample
542 largely reflects a heterogeneous distribution (segregation) of reactants, products, and retained
543 melt during biotite dehydration melting. The forward and reverse progression of the biotite
544 dehydration reactions resulted in a distinct layering that can be considered an example of
545 "metamorphic segregation" in gneissic rocks (Robin 1979; van der Molen 1985; Williams et al.
546 2000; Williams and Jercinovic 2002). It is perhaps understandable that the rheologically weak
547 and extractable melt component may be concentrated in distinct layers or removed to differing
548 degrees. It is interesting that the K-feldspar, a solid product of the melting reaction, forms
549 separate layers in the migmatite.

550 The strong layering and compositional segregation in sample 16TG143 may, at least in
551 part, be attributed to the tectonic (deformational) setting. As noted, the Rt. 22 outcrops occur
552 within a broad domain of top-to-the-east, normal shearing called the eastern Adirondack shear

zone. The outcrops sampled are not mylonitic and show little evidence of dynamic recrystallization or grain size reduction. However, the gneissic foliation is commonly deflected around garnet and feldspar crystals, and biotite overgrowths define asymmetric tails. The general non-coaxial flow combined with subtle modal (and thus rheological) heterogeneity in the migmatite would certainly have contributed to the production and enhancement of layering in the sample. Although beyond the scope of this paper, feedbacks between deformation, metamorphism, melting, and rheology are fundamentally important, particularly in these high-grade tectonites, and will be the subject of a further contribution.

The processes leading to compositional layering in the migmatite sample also influence the abundance of chronometers within the layers (Fig. 6a). Monazite and zircon are most abundant in Type 1 layers, interpreted to have undergone significant reversal of the melting reaction. Second in chronometer abundance are Type 3 layers, interpreted to contain a significant component of crystallized melt. Monazite and zircon are least abundant in Type 2 layers with abundant K-feldspar and garnet and little evidence of retrogression. Thus, monazite and zircon are most abundant in the layers interpreted to have retained at least some melt ($+H_2O$) during the melting event.

Yakymchuk (2017) modeled the behavior of monazite and apatite using an average metapelite composition that is almost identical to that of sample 16TG143 (Fig. 17) (Table S3). Monazite is calculated to dissolve into melt during prograde melting, although it may be preserved as inclusions in peritectic phases such as garnet. One significant observation is that at suprasolidus conditions, the isopleths of melt and monazite abundance are nearly vertical, and thus, largely temperature dependent. In the models, there is a wide range in temperature (~700 to 825 ºC) over which partial melting and monazite dissolution occurs. Likewise, the models

calculate a wide range over which monazite will precipitate, and melt will crystallize, during cooling (Yakymchuk 2017). For the following discussion, the general geometry of reaction boundaries and isopleths is considered to be applicable to 16TG143 given the similarity in bulk composition, although the exact location of the isopleths may differ somewhat due to the local water activity (Larson et al. 2022).

Petrochronologic Interpretations

Monazite Cores. Monazite grains from the non-leucosome portion of sample 16TG143 record three primary compositional domains: cores, mantles, and rims. Monazite cores have high Y and HREE in all layers (Fig. 8a, b). U-Pb dates from core domains range from ca. 1175-1150 Ma. These correspond with the later stages of the Shawinigan orogeny and AMCG magmatism. Williams et al. (2019) interpreted significant melting and garnet growth during this time in migmatitic samples located approximately 15 km west of the Rt. 22 locality based on a dramatic drop in Y and HREE in monazite. Notably, no comparable drop in Y at ca. 1150 Ma was observed at this time in this study.

We take the high Y and HREE in the cores to indicate that little or no garnet was present when the monazite cores crystallized. There is little evidence for the reactions that may have initially produced the high-Y monazite cores. The source of yttrium may have included the breakdown of phases, such as xenotime or allanite, during a lower-grade event (Spear and Pyle 2010). As discussed below, some muscovite dehydration melting may have occurred at this time. Monazite would likely maintain a relatively high Y content during muscovite dehydration melting because garnet is not a product of this reaction (Thompson 1982), and Y is predicted to favor monazite over melt (Stepanov et al. 2012). Nevertheless, the high Y and HREE content of

599 the core domains at Rt. 22 do not suggest significant garnet growth or biotite dehydration
600 melting at ca. 1150 Ma in this sample.

601 Although some high-Y cores are present in matrix monazite, cores in monazite inclusions
602 in garnet are larger, more euhedral, and more abundant. The presence of cores in a number of
603 matrix grains indicates that not all monazite was consumed during partial melting, i.e., the rocks
604 did not reach the monazite-out temperature. The fact that larger and less resorbed inclusions are
605 present in garnet also supports the interpretation that monazite was consumed during the melting
606 (garnet-growing) process. The metamorphic temperature reached approximately 800 ºC in this
607 sample based on the Zr-in-rutile thermometer (Kohn 2020). If the models of Yakymchuk (2017)
608 apply to this sample, as much as 80% of the monazite is predicted to have dissolved by 800 ºC
609 (Fig. 17c). We suggest that the cores underwent significant dissolution except where preserved
610 as matrix relics or inclusions in garnet (Fig. 18).

611 **Monazite Mantles.** Monazite mantles are the largest domains in most grains in all layers.
612 Compared to cores and rims, they are characterized by dramatically lower Y and HREE contents
613 (Fig. 8a, b). Mantle domains consistently yield ca. 1080-1050 Ma dates. We observe essentially
614 no examples of transitional (i.e., moderate-Y) domains between the cores and mantles. That is,
615 by the time that mantles began to grow, the Y and HREE were already substantially reduced.
616 This suggests that the mantles crystallized after significant garnet growth. The lack of
617 transitional compositions is consistent with the prediction that garnet grew on the prograde
618 (heating) path and that monazite mantles crystallized on the retrograde (cooling) path.

619 The monazite mantle domains are significantly depleted in U in addition to Y and HREE
620 (Fig. 8c). Stepanov et al. (2012) suggested that U will be partitioned from monazite into melt
621 more strongly than for most other trace elements and REEs. Therefore, if melt escapes from the

system, later monazite will be expected to have a reduced U content (Williams et al. 2019). Further, monazite in equilibrium with melt is expected to be depleted in uranium relative to other actinides or REEs (Williams et al. 2019). If the system remained closed with respect to melt, one would expect increasing U-content during the progressive crystallization of the mantle domains. We interpret the consistently low U abundance in the mantle domains to indicate that at least some melt was lost from the system prior to, or during monazite crystallization.

Additional evidence for the timing of monazite precipitation is provided by the dramatically increased S and Ca contents in mantle domains (Fig. 8e, f). In monazite, S may be accommodated as sulfate by the anhydrite substitution mechanism: $Ca^{2+} + S^{6+} = REE^{3+} + P^{5+}$ (Kukherenko et al. 1961; Krenn et al. 2011; Laurent et al. 2016). This substitution can explain the synchronous increase of Ca and S. Laurent et al. (2016) interpreted the increased S content in monazite from a granulite in Rogaland, Norway to be associated with partial melting; they suggested that the breakdown of Fe-sulfide and the subsequent sulfide oxidation are coeval with biotite dehydration melting.

We predict that monazite initially dissolves into melt during prograde heating above the solidus and then precipitates from the melt on cooling during progressive melt crystallization. The lack of monazite in Type 2 layers is consistent with the nearly total loss of melt from the layer. The results from the models indicate that approximately 80% of the monazite will crystallize between 825-750 ºC (Yakymchuk 2017) (Fig. 17c). The models also predict that only approximately half of the melt will have crystallized by 750 ºC, suggesting that abundant melt may be present during much of the monazite precipitation (Fig. 17b). Thus, we suggest that all of the monazite mantles in sample 16TG143 crystallized between temperatures of 800 to 750 ºC with melt present (Fig. 18).

The Yakymchuk (2017) monazite models assume a closed system. That is, the models do not incorporate melt loss or melt reintegration. Our results suggest that sample 16TG143 may have experienced some melt loss and that there may be differential melt retention in the different layer types. We expect that melt loss from the system would ultimately reduce the abundance of monazite that would crystallize on melt crystallization. At present, it is not possible to precisely predict the effect on all minor monazite components because partition coefficients are not well established. Components that are strongly partitioned into the melt relative to monazite (i.e., U) would be expected to be diminished, as we have observed (see below). Other elements, such as Y or REEs, that are not as strongly favored by melt would be less affected. While the absolute concentrations of these elements may be affected by melt loss, the overall calculated trends in dissolution and crystallization should remain largely unchanged. Therefore, we believe that the general conclusions of Yakymchuk's (2017) monazite modeling are still applicable to sample 16TG143 despite the possibility of melt loss.

Melt retained in the rock may participate in reversal of the melt reaction (progressive retrograde metamorphism) or it may crystallize to form a leucosome. Our observation for reversal of the biotite dehydration melting reaction suggest that the former may have occurred more readily in Type 1 layers and the latter in Type 3 layers, although certainly not exclusively so (Fig. 19). The controlling factors are not entirely clear, although we suspect that water content and the degree of melt escape (or melt gain) were contributing factors (Larson et al. 2022). The difference may help to explain the variation in monazite mantle texture between Type 1 and Type 3 layers. Monazite in Type 1 layers tends to have an irregular shape, commonly controlled by adjacent minerals such as garnet, indicating post garnet precipitation (Fig. 19). Type 3

667 monazite grains are generally euhedral, consistent with precipitation in a melt-rich(er)
668 environment (Taylor and Stevens 2010; Dorais and Tubrett 2012) (Fig. 19).

669 **Monazite rims.** Monazite rims are characterized by increased Y and HREE compared to
670 the mantles (Fig. 8a, b). The rim domains yield consistent ca. 1050-1000 Ma dates. The increases
671 in the Y and HREE are interpreted to result from garnet breakdown during continued cooling and
672 retrogression (Williams et al. 2019). Garnet is most abundant in Type 1 and 3 layers, and it is
673 also where we observe the highest Y and HREE content in monazite rims. Rims in Type 2 layers
674 have increased, but generally lower, Y and HREE abundance compared to layers Type 1 and 3.
675 Also, Type 2 rims yield nearly constant 1050 Ma dates; no younger (1050-1000 Ma) dates have
676 been obtained. The absence of young rims in Type 2 layers is consistent with the lack of
677 retrogression in the layers and the fact that monazite grains in Type 2 layers are mantled by K-
678 feldspar and thus, likely isolated from retrograde fluids.

679 Monazite rims in all layers are characterized by increasing uranium content (Fig. 8c). We
680 interpret the increase of U to reflect the final crystallization (or back reaction) of retained melt
681 (Fig. 18, 19). The lack of S and Ca in the rims is evidence that the rims precipitated in melt-
682 absent conditions, likely below the solidus. It is interesting that the U content of even the
683 youngest monazite rims remains elevated, well after melt is interpreted to have crystallized. We
684 suspect that U from late-stage melt or even hydrous fluids may be concentrated in grain
685 boundaries and may be available for incorporation into subsolidus monazite rims.

686

687 **Interpretation of zircon dates.** Zircon from the non-leucosome portion of sample
688 16TG143 are characterized by three domains/textures: cores, fir tree sector zoning, and rims.
689 Several cores yielded older 1250 Ma dates; however, most of the cores yielded an average of

1145 Ma (Fig. 15). The older cores may correspond with the Elzevirian orogeny (Rivers 2008). The ca. 1145 Ma grains correspond with the Shawinigan orogeny and the AMGC magmatic event. These probably resulted from the late Shawinigan metamorphism that has been documented in other parts of the eastern Adirondack Highlands (Williams et al. 2019). However, the grade was probably lower than in rocks to the north or west because little evidence exists for garnet growth at this time. If partial melting did occur, it probably involved muscovite dehydration melting, a reaction that does not involve garnet growth, but might result in zircon precipitation. Given the low abundance of older cores, we suggest this population largely dissolved into the 1050 Ma melt, consistent with interpretations from the monazite cores.

Most of the zircon grains are large (~100 μm) and round, with distinct fir tree texture (Fig. 15). The fir tree texture is a form of sector zoning that has been interpreted to reflect zircon crystallization during partial melting events (Raven and Dickson 1989; Corfu et al. 2003; Rubatto 2017) (Fig. 18, 19). The fir tree zircon grains yield an average date of 1045 Ma. Zircon abundance in the layers is similar to monazite, with zircon highest in Type 1 and 3 layers, layers interpreted to have retained some late-stage melt. Some zircon grains have thin (~5 μm) CL-bright rims. While these are too small to analyze by LA-ICP-MS, we suspect that the zircon rims reflect solid-state retrogression and subsolidus fluid interaction, presumably after ca. 1030 Ma, similar to the monazite rims (Fig. 18, 19).

Evidence for non-uniform heating-cooling during retrograde metamorphism

One important observation is that some monazite inclusions in garnet have low-Y, low HREE and ca. 1050 Ma dates. Many of these inclusions are cleanly preserved in garnet with no evidence of cracks, yet the grains still show low-Y (Fig. 10c). A simple heating-cooling path

713 combined with the modeling of Yakymchuk (2017) would suggest that garnet will crystallize
714 during progressive partial melting, and monazite will crystallize during progressive melt
715 crystallization. That is, monazite crystallization is expected to occur after garnet growth, and one
716 would not expect to find the low-Y monazite mantle inclusions in the peritectic garnet
717 porphyroblasts. As noted above, none of the mantles preserve transitional compositions (i.e.,
718 higher Y than typical mantles). Thus, garnet was already present when the inclusion mantles
719 crystallized. We take the ca. 1050 Ma low-Y inclusions in garnet to suggest some post-monazite
720 growth of garnet. One simple explanation involves transient heating and cooling cycles during
721 the overall cooling history. This would allow renewed garnet growth after some monazite
722 crystallization. Several workers have suggested that advective heating from mafic magmas may
723 have contributed to Ottawan metamorphism and if so, these would provide a mechanism for
724 transient heating (McLelland et al. 1996, 2001). Periods of additional heating would also help to
725 explain what seems to be a prolonged period of melt crystallization from ca. 1060 to ca. 1040 Ma
726 or younger (Wong et al. 2012; Williams et al. 2019; Mistikawy 2020; Pless 2020).

727 A second observation that may support the hypothesis of temperature reversals during the
728 overall cooling history involves the subtle U zoning in monazite mantles. Detailed microprobe
729 traverses across monazite mantles reveal subtle but systematic U zoning (Fig. 9). The U content
730 increases from core to rim as might be expected with progressive melt crystallization, but then
731 decreases either progressively or sharply only to steadily increase again. These subtle reversals
732 may represent periods of reheating and remelting, however, another possibility is that the
733 reversals represent periods of influx of more external melt into more local melt domains (Bea et
734 al. 2022). Both hypotheses may be related in that periods of reheating might involve enhanced
735 deformation and mixing of melt domains.

736

737 **The leucosome conundrum**

738 One complexity in our understanding of the gneissic layers in sample 16TG143 is the age
739 of the three-cm-thick (Type 4) leucosome layer. Our original hypothesis was that the Type 4
740 layer was produced and segregated during melting of the adjacent migmatitic gneiss (i.e., at ca.
741 1050 Ma). However, the petrochronologic results are more enigmatic. Core-mantle relationships
742 in zircon and monazite suggest two alternative possibilities: 1) the Type 4 layer may have been
743 produced at the time of monazite and zircon core crystallization (ca. 1150 Ma) and rims
744 represent metamorphic overgrowths or replacements or 2) the cores could be inherited grains in a
745 younger (ca. 1050 Ma) partial melt.

746 The difficulty in distinguishing between these two alternative interpretations prompted us
747 to collect the external leucosomes for comparison with the Type 4 layer. The external leucosome
748 and the Type 4 layer, while similar in appearance and bulk composition, have distinct differences
749 in the monazite/zircon characteristics. The external leucosomes preserve monazite with highly
750 enriched U content and dates that are exclusively ca. 1050 Ma and younger (Fig. 14c). No zircon
751 was recovered. The Type 4 layer preserves lower-U monazite with 1150 Ma cores and 1050 Ma
752 rims, and the monazite is extensively altered/reacted to apatite and extremely small U and Th-
753 rich inclusions (Fig. 6e). Further, ca. 1150 Ma zircon in the Type 4 layers have ca. 1050 Ma rims
754 with irregular boundaries, consistent with dissolution precipitation processes (Rubatto 2017)
755 (Fig. 16).

756 It is clear that the Type 4 leucosome and the external leucosomes differ in significant
757 ways, but it is not possible at present to definitively distinguish between the two hypotheses. It is
758 possible that the two types of leucosome were formed during separate metamorphic events or

759 during two different times in the same overall metamorphic cycle, possibly originating from
760 different source rocks. However, we tentatively favor the first hypothesis, that the Type 4 layer
761 was produced during an older (ca. 1150 Ma) melting event and was incorporated into our sample
762 and then metamorphosed, deformed, and altered in the ca. 1050 Ma Ottawan event. The external
763 leucosomes, we suggest, were produced during the younger (ca. 1050 Ma) melting event. We
764 base these preferences on: (1) the lack of 1150 Ma monazite or zircon in the external
765 leucosomes; (2) the lack of fir-tree texture zircon and the presence of dissolution-reprecipitation
766 texture in Type 4 zircon; (3) the alteration/metamorphism of Type 4 monazite; and (4) the
767 relative lack (although not exclusively so) of inherited monazite in igneous rocks in general due
768 to dissolution in melt. Our final conclusion is that in sample 16TG143, the restitic migmatite
769 layers provide much firmer evidence for ca. 1050 (Ottawan) melting than the leucosome layers.
770

771 **Tectonic implications**

772 The two main granulite-facies events recognized in the Adirondack Highlands are the
773 1190-1140 Ma Shawinigan orogeny and the 1090-1020 Ma Ottawan orogeny (Rivers 2008;
774 McLelland et al. 2013; Chiarenzelli et al. 2017; Williams et al. 2019). Extensive biotite
775 dehydration melting and garnet growth have been interpreted in several parts of the Adirondack
776 Highlands during the later stages of the Shawinigan event (ca. 1160-1150 Ma) (Heumann et al.
777 2006; Bickford et al. 2008; Williams et al. 2019; Pless 2020), which would correlate with our
778 1150 Ma monazite and zircon cores. However, data from sample 16TG143 indicates little or no
779 garnet growth at 1150 Ma. If there was any melting at all, it probably involved muscovite
780 dehydration, implying a lower grade of metamorphism during the late Shawinigan. This is
781 consistent with growing evidence that the Shawinigan event was heterogeneous in metamorphic

782 conditions and timing (see also Mistikawy 2020), but more regional petrochronology will be
783 required to define the nature of any metamorphic field gradients.

784 The 1090-1020 Ma Ottawan orogeny is also interpreted to have resulted in granulite
785 facies conditions throughout the Adirondack Highlands (Rivers 2008). Petrochronologic results
786 from the monazite mantle domains and the fir tree zircon in sample 16TG143 provide evidence
787 for extensive biotite dehydration melting and substantial garnet growth at ca. 1065-1050 Ma.
788 Notably, the geochronometers from the Rt. 22 locality do not record a prograde metamorphic
789 history leading to the Ottawan peak conditions. Instead, monazite and zircon record the timing of
790 progressive cooling from peak metamorphic conditions (800 °C, 0.8 GPa) to final melt
791 crystallization (~700 °C) (Fig. 18).

792 Recent studies suggest that temperatures in the Ottawan event may have reached ultra-
793 high temperature conditions (UHT) in some parts of the Adirondack Highlands (Ferrero et al.
794 2021; Metzger et al. 2021). However, our thermobarometry, phase relationships, and the
795 presence of relict monazite and zircon, support a peak temperature of approximately 800 °C at
796 the Rt 22 locality, well below UHT conditions. The Rt. 22 locality is located at the edge of the
797 Adirondack uplift, and previous workers have suggested a concentric (Bulls-eye) isograd pattern
798 (Bohlen et al. 1985; Spear and Markesson 1997). It is possible that hotter conditions prevailed
799 nearer to the center of the Highlands terrane.

800 The Rt 22 locality has been previously interpreted as part of the eastern Adirondack shear
801 zone that accommodated extensional collapse during the late Ottawan (Wong et al. 2012; Regan
802 et al. 2019; Williams et al. 2019). We suggest that cooling, garnet breakdown, and retrogression
803 occurred between ca. 1050 to 1000 Ma, consistent with the interpreted timing of decompression
804 in the Adirondack Highlands. We do not find evidence for significant heating after ca. 1050 Ma;

805 however, the abundance of ca. 1030 Ma pegmatites and quartz veins in the region is evidence for
806 extensive hydrothermal processes (Valley et al. 2011).
807
808 **Broader Implications**
809 Gneissic layering is a common characteristic of high-grade metamorphic rocks. The
810 layering is commonly attributed to "metamorphic segregation" but the specific mechanisms for
811 developing the segregations are less clear (Robin 1979; van der Molen 1985; Williams et al.
812 2000; Williams and Jercinovic 2002). Partial melting certainly can play a role, and some gneissic
813 layers are clearly related to the melt component. However, our observations suggest that other
814 layers are related to the differential preservation of solid-state reactants and products of the
815 melting reaction and also to differing retrograde reactions involving the melt component. Some
816 aspects of the layering, such as the development of nearly pure K-feldspar + garnet layers remain
817 subjects for further analysis. However, correlations between the gneissic layering and character
818 and composition of geochronometers emphasize the importance of understanding the layer-
819 forming processes as a critical part of deconvoluting the timing and history of gneissic rocks.
820 Dating leucosome layers would seem to be an obvious first step in constraining the age of
821 high-grade migmatitic rocks. However, constraining the age of leucosome layers (Type 4 and
822 external) at the Rt 22 locality is far from straightforward. We suggest that the Type 4 layer
823 represents early melting at ca. 1150 Ma, while the external leucosomes likely represent melting
824 at ca. 1050 Ma, but we must admit that the data are not conclusive. The timing of melting could
825 be misinterpreted if only the leucosome layers were analyzed from this outcrop. In sample
826 16TG143, the Type 1 migmatitic layers preserve the complete monazite and zircon petrogenesis
827 record. The results from our study highlight the significance of carefully analyzing all layers of a

828 migmatite combined with grain mapping and in-situ petrochronology in order to characterize the
829 tectonic history, especially in regions that have experienced multiple tectono-thermal events.
830

831 **Acknowledgments**

832 We thank Ian Hillenbrand and Justin Mistikawy for their thorough reviews of an earlier
833 version of the paper. We thank Greg Walsh, Peter Valley, Marian Lupulescu, Meghan Toft, Dan
834 Tjapkes, and Victor Guevara for helpful discussions. We appreciate the constructive and
835 thoughtful reviews of Stacia Gordon, Besim Dragovic, Kyle Larson, and we thank Edward Grew
836 for editorial support. We acknowledge Bruce Selleck and Jim McLelland for decades
837 of foundational work in the Adirondack Mountains. Funding for this project came, in part, from
838 NSF Grant EAR-1419876 to Williams and Grover and the NSF Graduate Research Fellowship
839 Award 1451512 to Suarez. Finally, this manuscript is dedicated in memory of Sheila Seaman, a
840 cherished mentor, educator, and petrologist.
841

842 Allaz, J.M., Williams, M.L., Jercinovic, M.J., Goemann, K., and Donovan, J. (2019) Multipoint
843 background analysis: Gaining precision and accuracy in microprobe trace element analysis.
844 Microscopy and Microanalysis, 25, 30–46.
845 Bickford, M.E., McLelland, J.M., Selleck, B.W., Hill, B.M., and Heumann, M.J. (2008) Timing
846 of anatexis in the eastern Adirondack Highlands: Implications for tectonic evolution during
847 ca. 1050 Ma Ottawan orogenesis. Bulletin of the Geological Society of America, 120, 950–
848 961.
849 Chiarenzelli, J.R., Selleck, B.W., Lupulescu, M. V., Regan, S.P., Bickford, M.E., Valley, P.M.,
850 and McLelland, J.M. (2017) Lyon Mountain ferroan leucogranite suite: Magmatic response
851 to extensional thinning of overthickened crust in the core of the Grenville orogen.
852 Geological Society of America Bulletin, 129, 1472–1488.
853 Dumond, G., McLean, N., Williams, M.L., Jercinovic, M.J., and Bowring, S.A. (2008) High-
854 resolution dating of granite petrogenesis and deformation in a lower crustal shear zone:
855 Athabasca granulite terrane, western Canadian Shield. Chemical Geology, 254, 175–196.
856 Ferrero, S., Wannhoff, I., Laurent, O., Yakymchuk, C., Darling, R., Wunder, B., Borghini, A.,
857 and O'Brien, P.J. (2021) Embryos of TTGs in Gore Mountain garnet megacrysts from
858 water-fluxed melting of the lower crust. Earth and Planetary Science Letters, 569.
859 Gehrels, G.E., Valencia, V.A., and Ruiz, J. (2008) Enhanced precision, accuracy, efficiency, and
860 spatial resolution of U-Pb ages by laser ablation-multicollector-inductively coupled plasma-
861 mass spectrometry. Geochemistry, Geophysics, Geosystems, 9.
862 Heumann, M.J., Bickford, M.E., Hill, B.M., McLelland, J.M., Selleck, B.W., and Jercinovic,
863 M.J. (2006) Timing of anatexis in metapelites from the Adirondack lowlands and southern
864 highlands: A manifestation of the Shawinigan orogeny and subsequent anorthosite-

mangerite-charnockite-granite magmatism. Bulletin of the Geological Society of America, 118, 1283–1298.

Jercinovic, M.J., Williams, M.L., and Lane, E.D. (2008) In-situ trace element analysis of monazite and other fine-grained accessory minerals by EPMA. Chemical Geology, 254, 197–215.

Larson, K.P., Shrestha, S., Cottle, J.M., Guilmette, C., Johnson, T.A., Gibson, H.D., and Gervais, F. (2022) Re-evaluating monazite as a record of metamorphic reactions. Geoscience Frontiers, 13.

McLelland, J., and Wong, M. (2008) Geology and Geochronology of the Eastern Adirondacks. New York State Geological Association Field Trip Guide Trip B1.

McLelland, J.M., Bickford, M.E., Hill, B.M., Clechenko, C.C., Valley, J.W., and Hamilton, M.A. (2004) Direct dating of Adirondack massif anorthosite by U-Pb SHRIMP analysis of igneous zircon: Implications for AMCG complexes. Bulletin of the Geological Society of America, 116, 1299–1317.

McLelland, J.M., Selleck, B.W., and Bickford, M.E. (2013) Tectonic Evolution of the Adirondack Mountains and Grenville Orogen Inliers within the USA. Geoscience Canada, 40, 318.

Metzger, E.P., Leech, M.L., Davis, M.W., Reeder, J. v., Swanson, B.A., and Waring, H. v. (2022) Ultrahigh-temperature granulite-facies metamorphism and exhumation of deep crust in a migmatite dome during late- to post-orogenic collapse and extension in the central Adirondack Highlands (New York, USA). Geosphere, 18, 261–297.

Mezger, K., van der Pluijm, B.A., Essene, E.J., and Halliday, A.N. (1992) The Carthage-Colton Mylonite Zone (Adirondack Mountains, New York): The Site of a Cryptic Suture in the Grenville Orogen?, 630–638 p. Source: The Journal of Geology Vol. 100.

Miriam L. Fuhrman, and Donald H. Lindsley (1988) Ternary-feldspar modeling and thermometry, 201–215 p. American Mineralogist Vol. 73.

Montel, J.M., Foret, S., Veschambre, M., Nicollet, C., and Provost, A. (1996) Electron Microprobe dating of monazite. Chemical Geology, 131, 37–53.

Regan, S.P., Chiarenzelli, J.R., Mclelland, J.M., Cousens, B.L., Regan, S.P., Chiarenzelli, J.R., Mclelland, J.M., and Cousens, B.L. (2011) Evidence for an enriched asthenospheric source for coronitic metagabbros in the Adirondack Highlands.

Regan, S.P., Geer, P., Walsh, G.J., Aleinikoff, J., Valley, P., Williams, M., Jercinovic, M., and Grover, T. (2015) Precambrian geology of the Eagle Lake quadrangle, Essex County, New York. New York State Geological Association.

Regan, S.P., Walsh, G.J., Williams, M.L., Chiarenzelli, J.R., Toft, M., and McAleer, R. (2019) Syn-collisional exhumation of hot middle crust in the Adirondack Mountains (New York, USA): Implications for extensional orogenesis in the southern Grenville province. Geosphere, 15, 1240–1261.

Rivers, T. (1997) Lithotectonic Elements of the Grenville Province: review and tectonic implications, 86, 117–154.

Rivers, T., and Volkert, R. A. (2023) Slow cooling in the metamorphic cores of Grenvillian large metamorphic core complexes and the thermal signature of the Ottawan orogenic lid. Laurentia: Turning Points in the Evolution of a Continent, Steven J. Whitmeyer, Michael L. Williams, Dawn A. Kellett, Basil Tikoff

Schoene, B., Condon, D.J., Morgan, L., and McLean, N. (2013) Precision and accuracy in geochronology. Elements, 9, 19–24.

Selleck, B.W., McLelland, J.M., and Bickford, M.E. (2005) Granite emplacement during tectonic exhumation: The Adirondack example. Geology, 33, 781–784.

Spear, F.S., and Markussen, J.C. (1997) Mineral zoning, P-T-X-M phase relations, and metamorphic evolution of some Adirondack granulites, New York. Journal of Petrology, 38, 757–783.

Storm, L.C., and Spear, F.S. (2005) Pressure, temperature and cooling rates of granulite facies migmatitic pelites from the southern Adirondack Highlands, New York. Journal of Metamorphic Geology, 23, 107–130.

Swanson-Hysell, N.L. (2021) The Precambrian paleogeography of Laurentia. In Ancient Supercontinents and the Paleogeography of Earth pp. 109–153. Elsevier.

Valley, P.M., Hanchar, J.M., and Whitehouse, M.J. (2011) New insights on the evolution of the Lyon Mountain Granite and associated Kiruna-type magnetite-apatite deposits, Adirondack Mountains, New York State. Geosphere, 7, 357–389.

Williams, M.L., Melis, E.A., Kopf1, C.F., and Anmer2, A.D.S.H. (2000) Microstructural tectonometamorphic processes and the development of gneissic layering: a mechanism for metamorphic segregation, 41–57 p. J. metamorphic Geol Vol. 18.

Williams, M.L., Jercinovic, M.J., Goncalves, P., and Mahan, K. (2006) Format and philosophy for collecting, compiling, and reporting microprobe monazite ages. Chemical Geology, 225, 1–15.

Williams, M.L., Jercinovic, M.J., Mahan, K.H., and Dumond, G. (2017) Electron Microprobe Petrochronology. Reviews in Mineralogy and Geochemistry, 83, 153–182.

Williams, M.L., Grover, T., Jercinovic, M.J., Regan, S.P., Pless, C.R., and Suarez, K.A. (2019) Constraining the timing and character of crustal melting in the Adirondack Mountains using multi-scale compositional mapping and in-situ monazite geochronology. American Mineralogist, 104, 1585–1602.

Wong, M.S., Williams, M.L., McLelland, J.M., Jercinovik, M.J., and Kowalkoski, J. (2012) Late Ottawan extension in the eastern Adirondack Highlands: Evidence from structural studies and zircon and monazite geochronology. Bulletin of the Geological Society of America, 124, 857–869.

Yakymchuk, C. (2023) Prograde zircon growth in migmatites. Journal of Metamorphic Geology.

Figure 1: A) Location of the Adirondack Mountains in relation to the North American Grenville Province (after Mistikawy, 2020). B) Generalized geologic map of the Adirondack Mountains (after McLelland et al. 2013; Taylor et al., 2019). Green color shows the location of metasedimentary rocks. C) Location of the outcrop along Rt. 4/22 from which the samples were taken for this study (43º 27’ 57” N, 73º 26’ 24” W).

948 Figure 2: Cut face of sample 16TG143, the main focus of this study. Five polished sections (as
949 shown) were prepared in attempt to characterize all layers of the migmatite.
950
951 Figure 3: (a) Photo of one billet from migmatitic gneiss in sample 16TG143-3 with major
952 minerals (Kfs, Bt, Gt, Pl) labeled. (b-d) Full-thin-section compositional maps. Brighter colors
953 indicate higher abundance of the particular element. Major minerals are noted in each map. Maps
954 were collected with pixel size = 35 mm, current = 300 nA, dwell time = 20 ms.
955
956 Figure 4: Interpreted layer types (Types 1-4) in sample 16TG143. See text for discussion.
957
958 Figure 5: (a) Reflected light photo of layer types (1-3) in the grey gneiss. Locations for B-D are
959 included. (b) Cross-polarized photomicrograph of garnet in Type 1 layers (left) and generalized
960 sketch of the minerals (right). (c) Cross-polarized photomicrograph of garnet in Type 2 layers
961 (left) and generalized sketch of the minerals (right). (3) Cross-polarized photomicrograph of
962 garnet in Type 3 layers (left) and generalized sketch of the minerals (right).
963
964 Figure 6: (a) Distribution of monazite and zircon in Type 1-3 layers. Locations for B-D are
965 included. (b) Monazite textures in Type 1 layers are somewhat controlled by adjacent minerals,
966 such as biotite. (c) Type 2 monazite is subhedral to euhedral (d) Monazite in Type 3 layers is
967 euhedral (e) Type 4 monazite grains have fine U and Th-rich inclusions and apatite near rims
968 (see inset). (f) External leucosome grains are equant in shape with no apparent alteration.
969
970 Figure 7: (a) Gaussian distribution showing all monazite dates from the Type 1-3 layers. Each
971 distribution curve represents one monazite domain, typically one background analysis and 6 peak

972 measurements. Inset: monazite yttrium composition for a grain in the grey gneiss with a core,
973 mantle, and rim. (b) Yttrium vs. date for monazite analyses from Fig. 7a.
974
975 Figure 8: Monazite results from the Type 1-3 layers. (a) Yttrium vs. date (b) Sum of the Heavy
976 Rare Earth Elements vs. date (c) Uranium vs. date (d) Thorium vs. date (e) Sulfur vs. date (f)
977 Calcium vs. date. Horizontal scales are equal in all figures.
978
979 Figure 9: Uranium transverse across a representative mantle domain with increasing and
980 decreasing U content. Inset: monazite uranium composition for a single grain in sample
981 16TG143 with mantle traverse location.
982
983 Figure 10: (a) Yttrium vs. date for the monazite inclusions in garnet. (b) Monazite inclusion in
984 garnet (left) and monazite grain map showing high yttrium content (right) (b) Monazite inclusion
985 in garnet (left) and monazite grain map showing low yttrium content (right).
986
987 Figure 11: (a) Gaussian distribution showing all monazite dates from the Type 4 layer. Each
988 distribution curve represents one monazite domain, typically one background analysis and 6 peak
989 measurements. Inset: Monazite yttrium compositional map for one grain in the Type 4
990 leucosome layer showing core, mantle, and rim. (b) (c) Yttrium vs. date for monazite analyses
991 from Fig. 11a.
992

Figure 12: Monazite results from the Type 4 (leucosome) layer. (a) Yttrium vs. date (b) Sum of the Heavy Rare Earth Elements vs. date (c) Uranium vs. date (d) Thorium vs. date (e) Sulfur vs. date (f) Calcium vs. date. Horizontal scales are equal in all figures.

Figure 13: (a) Gaussian distribution showing all the monazite dates from the external leucosomes. Each distribution curve represents one monazite domain, typically one background analysis and 6 peak measurements. Inset: monazite yttrium compositions for grains in the external leucosomes. Zoned grains have a core, mantle, and rim. Unzoned grains have high or low yttrium content. (b) Yttrium vs. date for monazite analyses from Fig. 13a.

Figure 14: Monazite results from external leucosome samples. (a) Yttrium vs date (b) Sum of the Heavy Rare Earth Elements vs. date (c) Uranium vs. date. (d) Thorium vs. date. (e) Sulfur vs. date (f) Calcium vs. date. Horizontal scales are equal in all figures.

Figure 15: Zircon results from Type 1-3 layers. Concordia diagram ($^{206}Pb/^{238}U$ vs. $^{207}Pb/^{235}U$) showing Laser Ablation ICP Mass Spectrometry zircon U-Th-Pb zircon dates. Error ellipses are 2σ. Inset: typical zircon with fir-tree sector zoning texture.

Figure 16: Zircon results from the Type 4 layer. Concordia diagram ($^{206}Pb/^{238}U$ vs. $^{207}Pb/^{235}U$) showing Laser Ablation ICP Mass Spectrometry zircon U-Th-Pb zircon dates. Error ellipses are 2σ. Inset: typical zircon with oscillatory zoned core and CL-bright rim.

Figure 17: (a) P–T pseudosection for an average metapelite. (b) Contours for the proportion of anatectic melt in mol.% in the metapelite in a closed system. (c) Contours for the amount of monazite dissolution (%) in a closed system, including apatite using the Wolf and London (1994) apatite solubility equation (see Yakymchuk 2017). The dashed line is the solidus. The star marks the interpreted P–T conditions for sample 16TG143. Modified with permission from Yakymchuk 2017.

Figure 18: Schematic P–T path for the Rt. 22 migmatite. Monazite and zircon dissolution occurs on the prograde path. Monazite mantles and fir tree zircon crystallize on the cooling path. Episodic reheating may have occurred. See text for discussion. Subsolidus retrograde reactions are interpreted to result in the precipitation of rims on both monazite and zircon.

Figure 19: Model for development of the compositional layers and petrogenesis of geochronometers in sample 16TG143 during biotite dehydration melting. Type 1 layers underwent reversal of the biotite dehydration melting reaction. Type 2 layers are dominated by K-feldspar, a solid product of the melting reaction. Type 3 layers retained a significant portion of crystallized melt. The Type 4 layer is a quartz, feldspar leucosome that is interpreted to represent earlier melting (see text for discussion).

Figure S1: Photo of the outcrop along Rt. 4/22 showing the relationship between the migmatitic rocks (sample 16TG143) and the external leucosome layers (17W001 and 17W002).

This is the peer-reviewed, final accepted version for American Mineralogist, published by the Mineralogical Society of America.
The published version is subject to change. Cite as Authors (Year) Title. American Mineralogist, in press.
DOI: https://doi.org/10.2138/am-2022-8679. http://www.minsocam.org/

Table 1. Modes of Major Minerals

Mineral	Type 1a	Type 1b	Type 2	Type 3	Type 4	External
Garnet	25	35	5	15	5	5
K-feldspar	28	16	50	3	37	30
Plagioclase	17	25	2	60	29	25
Quartz	20	10	41	18	28	34
Sillimanite	5	7	1	2	0	5
Biotite	5	7	1	2	1	1

1037

Table 2. Temperature and Pressure Estimates

Method	All Layers	Type 1	Type 2-4	External
Zr-in-Rutile	800 °C	-	-	-
Ti-in-Biotite	-	700 °C	725 °C	725 °C
GASP	0.8 GPa	-	-	-

1038

Table 3. Approximate Modes of Monazite and Zircon per cm^2

Mineral	Type 1a	Type 1b	Type 2	Type 3	Type 4	External
Monazite	8	17	2	6	4	1
Zircon	10	23	4	7	9	1

This is the peer-reviewed, final accepted version for American Mineralogist, published by the Mineralogical Society of America.
The published version is subject to change. Cite as Authors (Year) Title. American Mineralogist, in press.
DOI: https://doi.org/10.2138/am-2022-8679. http://www.minsocam.org/

Fig. 1

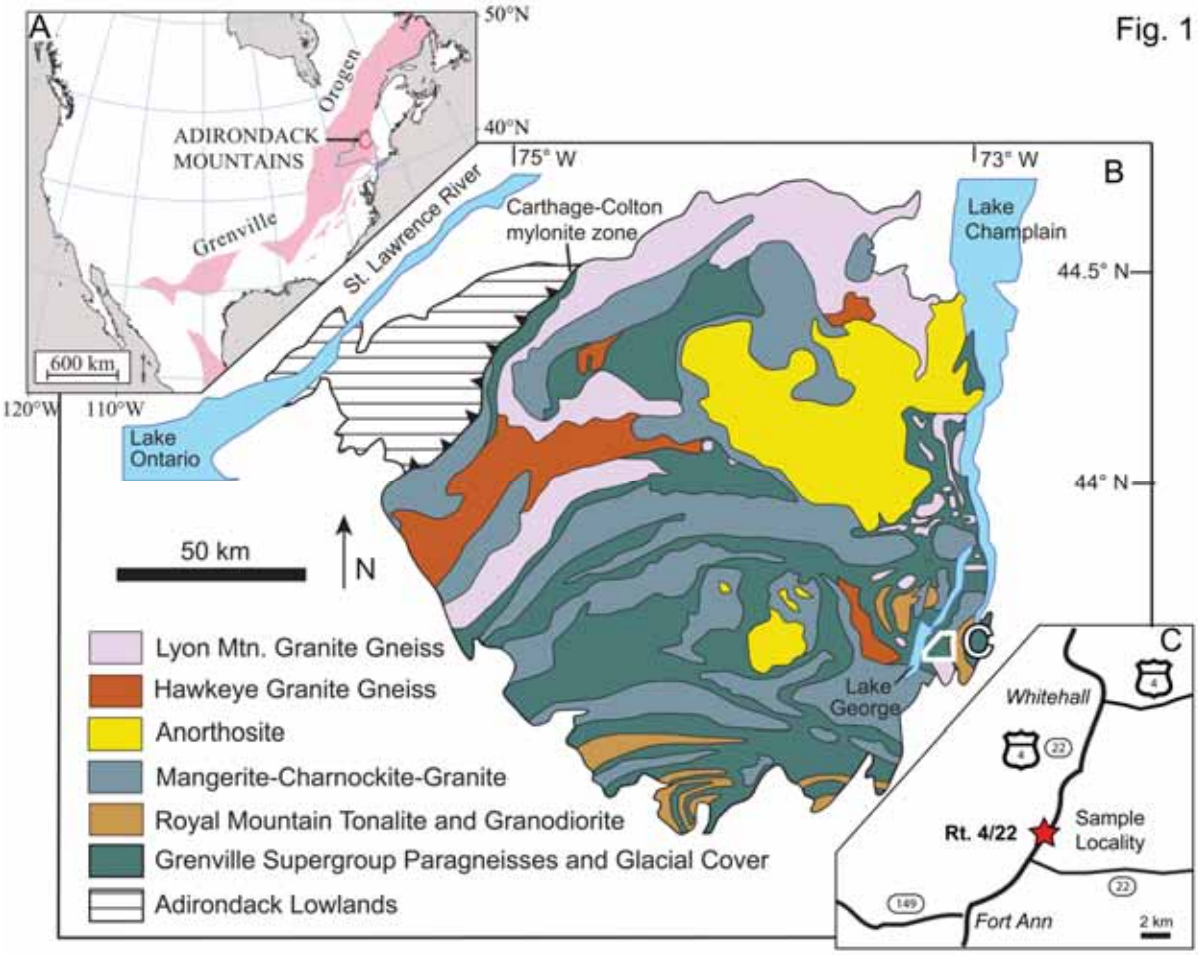

1039

Fig. 2

1040

This is the peer-reviewed, final accepted version for American Mineralogist, published by the Mineralogical Society of America.
The published version is subject to change. Cite as Authors (Year) Title. American Mineralogist, in press.
DOI: https://doi.org/10.2138/am-2022-8679. http://www.minsocam.org/

1041

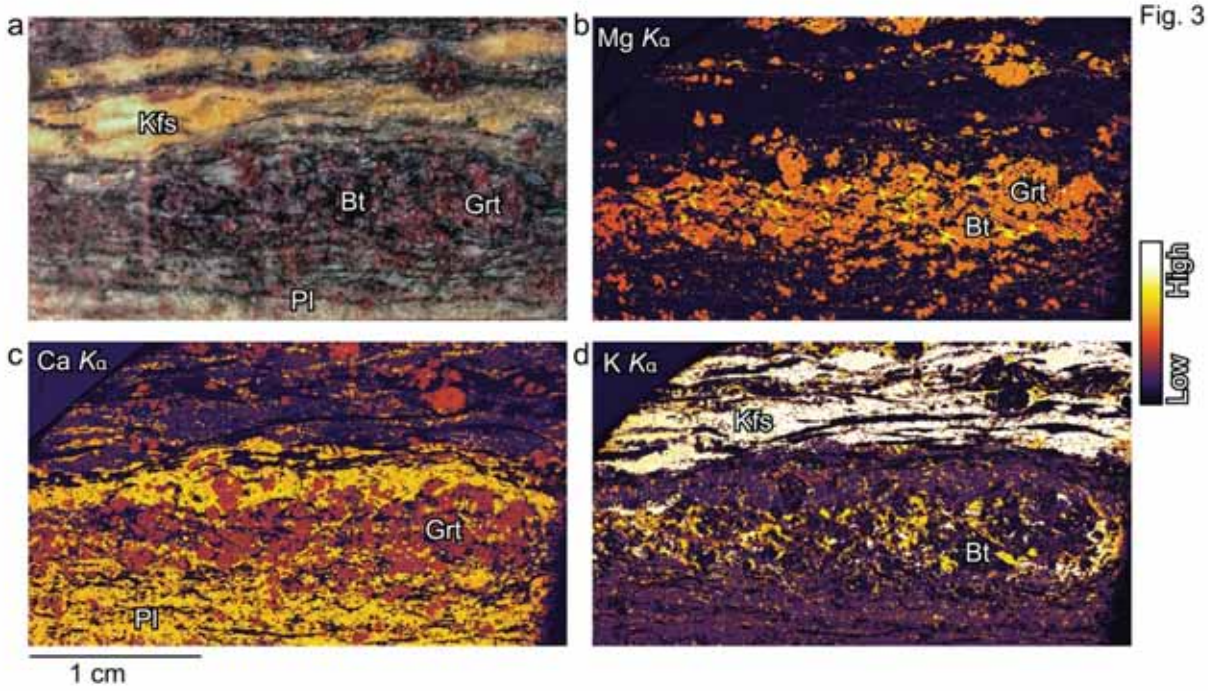

Fig. 3

1042

This is the peer-reviewed, final accepted version for American Mineralogist, published by the Mineralogical Society of America.
The published version is subject to change. Cite as Authors (Year) Title. American Mineralogist, in press.
DOI: https://doi.org/10.2138/am-2022-8679. http://www.minsocam.org/

Fig. 4

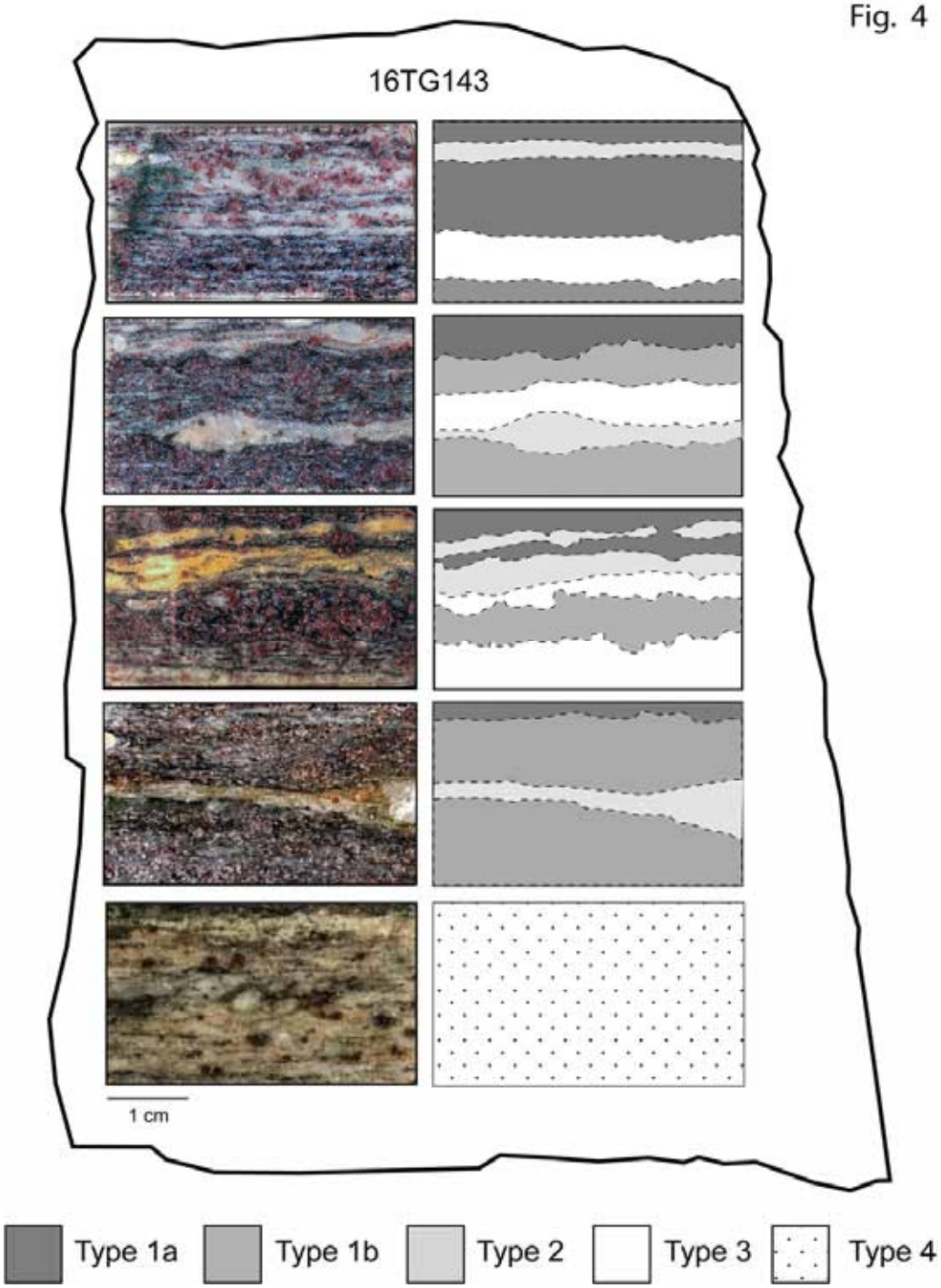

This is the peer-reviewed, final accepted version for American Mineralogist, published by the Mineralogical Society of America.
The published version is subject to change. Cite as Authors (Year) Title. American Mineralogist, in press.
DOI: https://doi.org/10.2138/am-2022-8679. http://www.minsocam.org/

Fig. 5

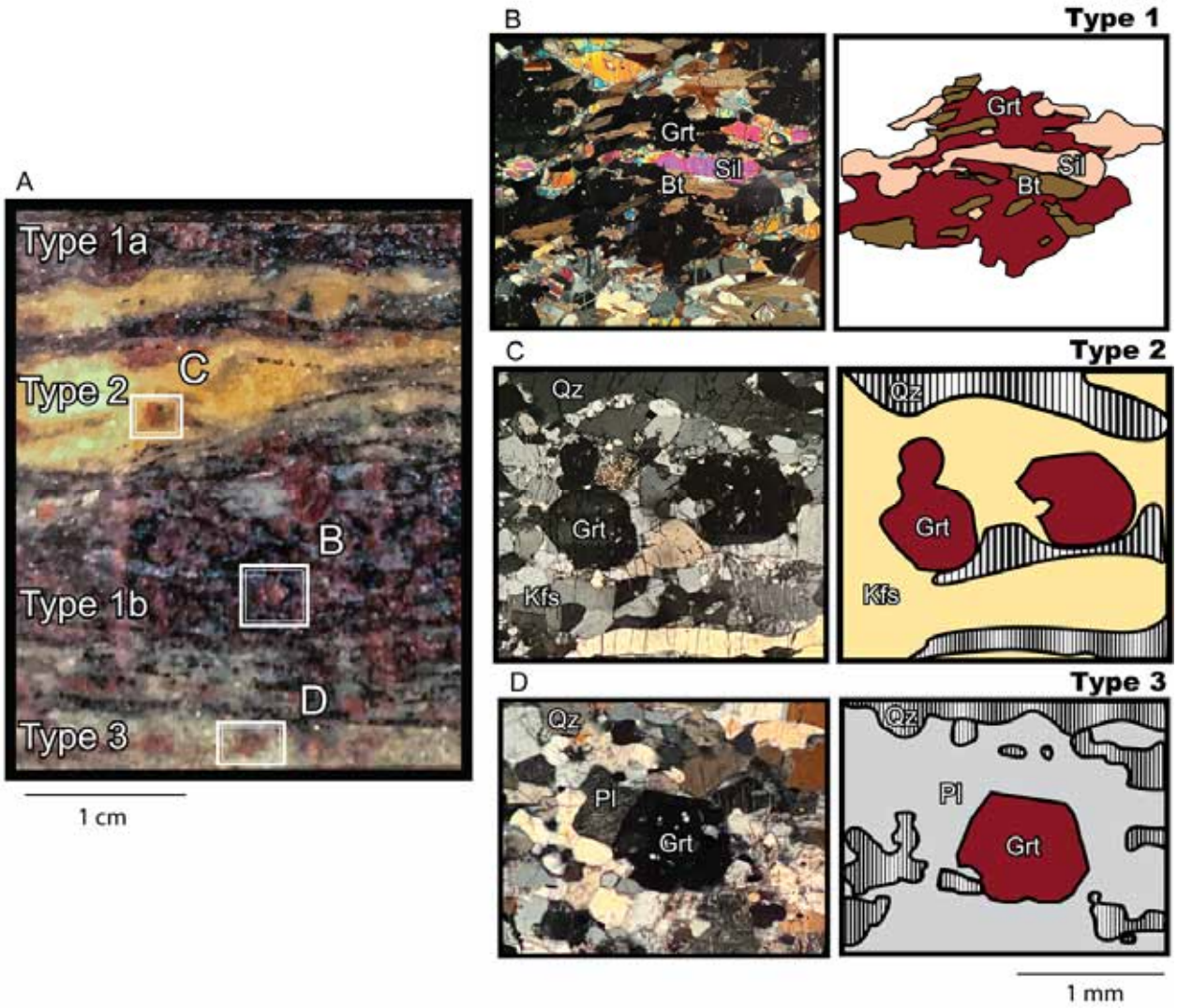

1047

This is the peer-reviewed, final accepted version for American Mineralogist, published by the Mineralogical Society of America.
The published version is subject to change. Cite as Authors (Year) Title. American Mineralogist, in press.
DOI: https://doi.org/10.2138/am-2022-8679. http://www.minsocam.org/

Fig. 6

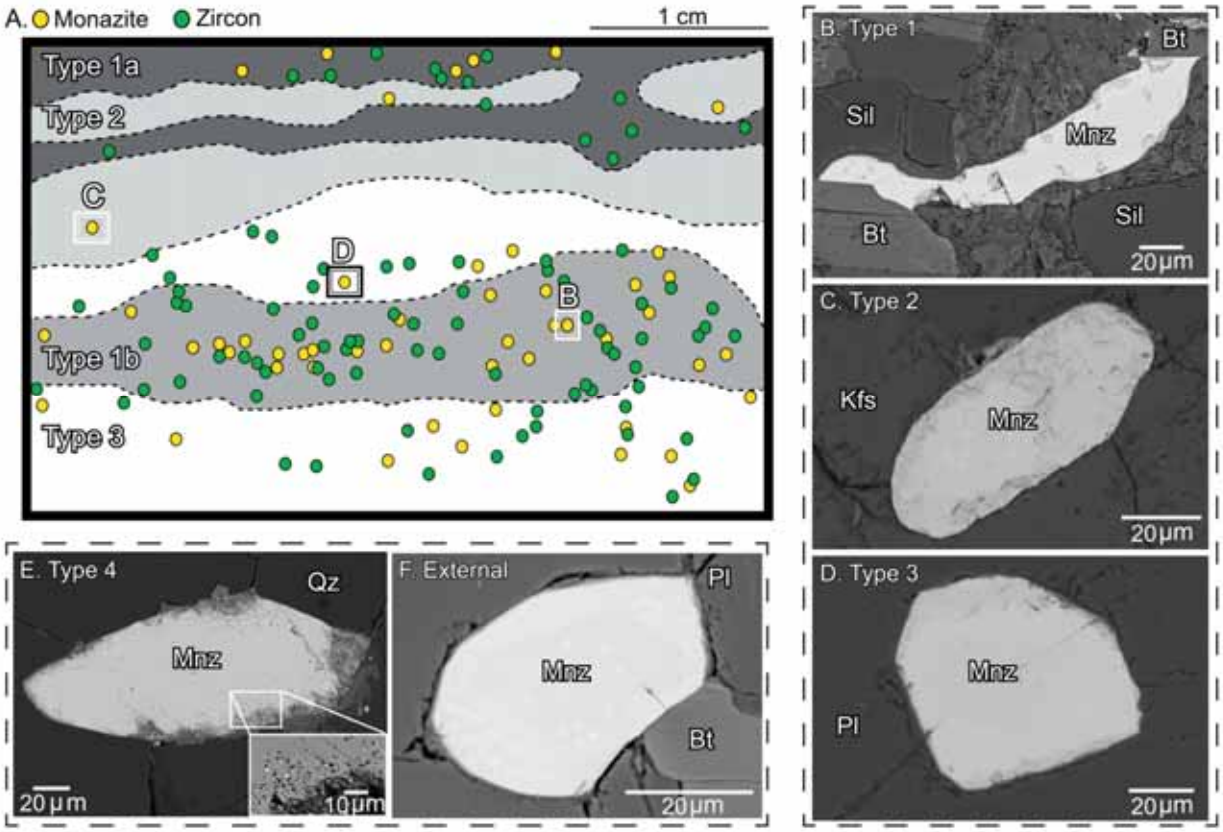

1048

This is the peer-reviewed, final accepted version for American Mineralogist, published by the Mineralogical Society of America.
The published version is subject to change. Cite as Authors (Year) Title. American Mineralogist, in press.
DOI: https://doi.org/10.2138/am-2022-8679. http://www.minsocam.org/

Fig. 7

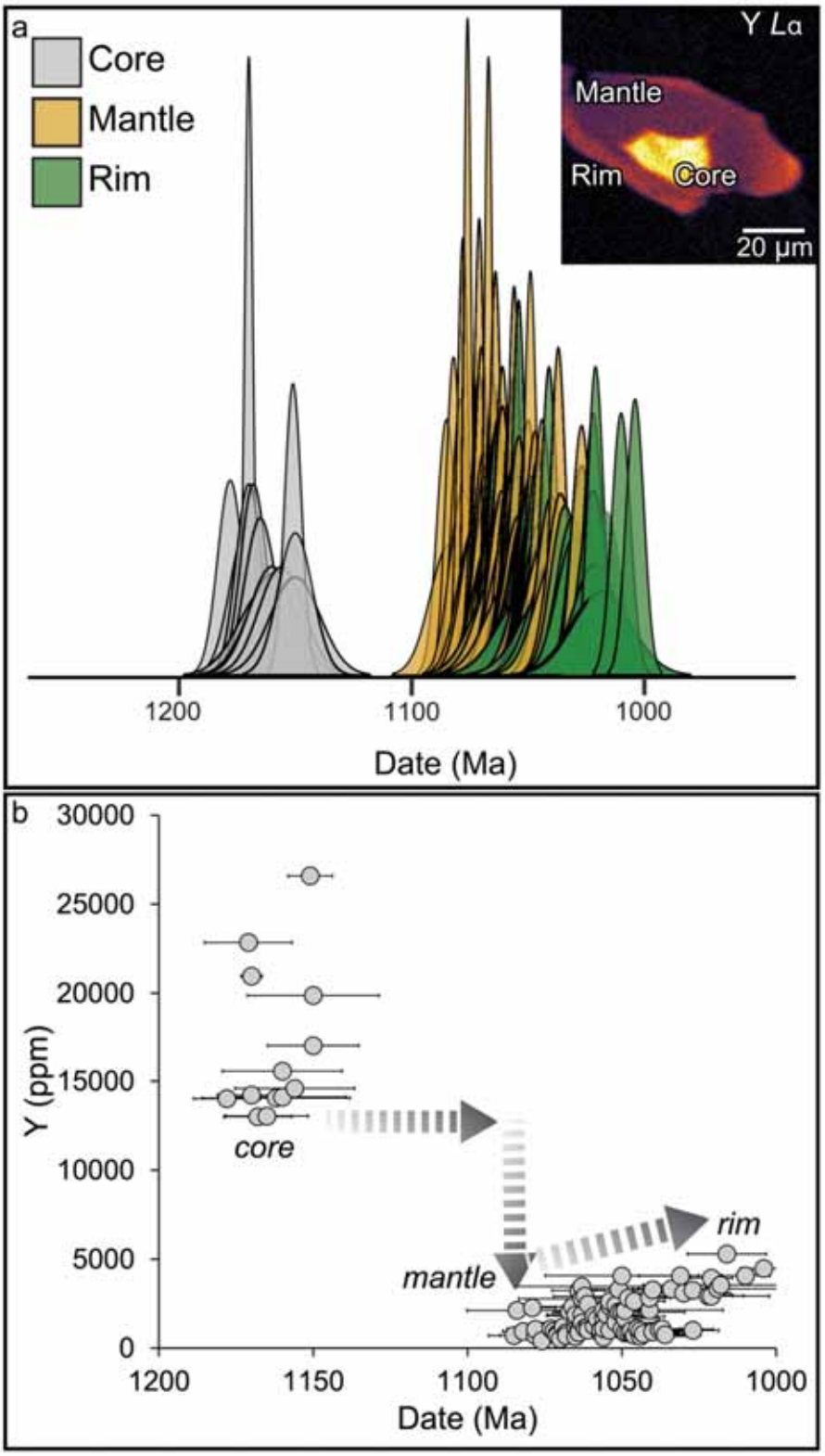

1049

This is the peer-reviewed, final accepted version for American Mineralogist, published by the Mineralogical Society of America.
The published version is subject to change. Cite as Authors (Year) Title. American Mineralogist, in press.
DOI: https://doi.org/10.2138/am-2022-8679. http://www.minsocam.org/

1050

Fig. 8

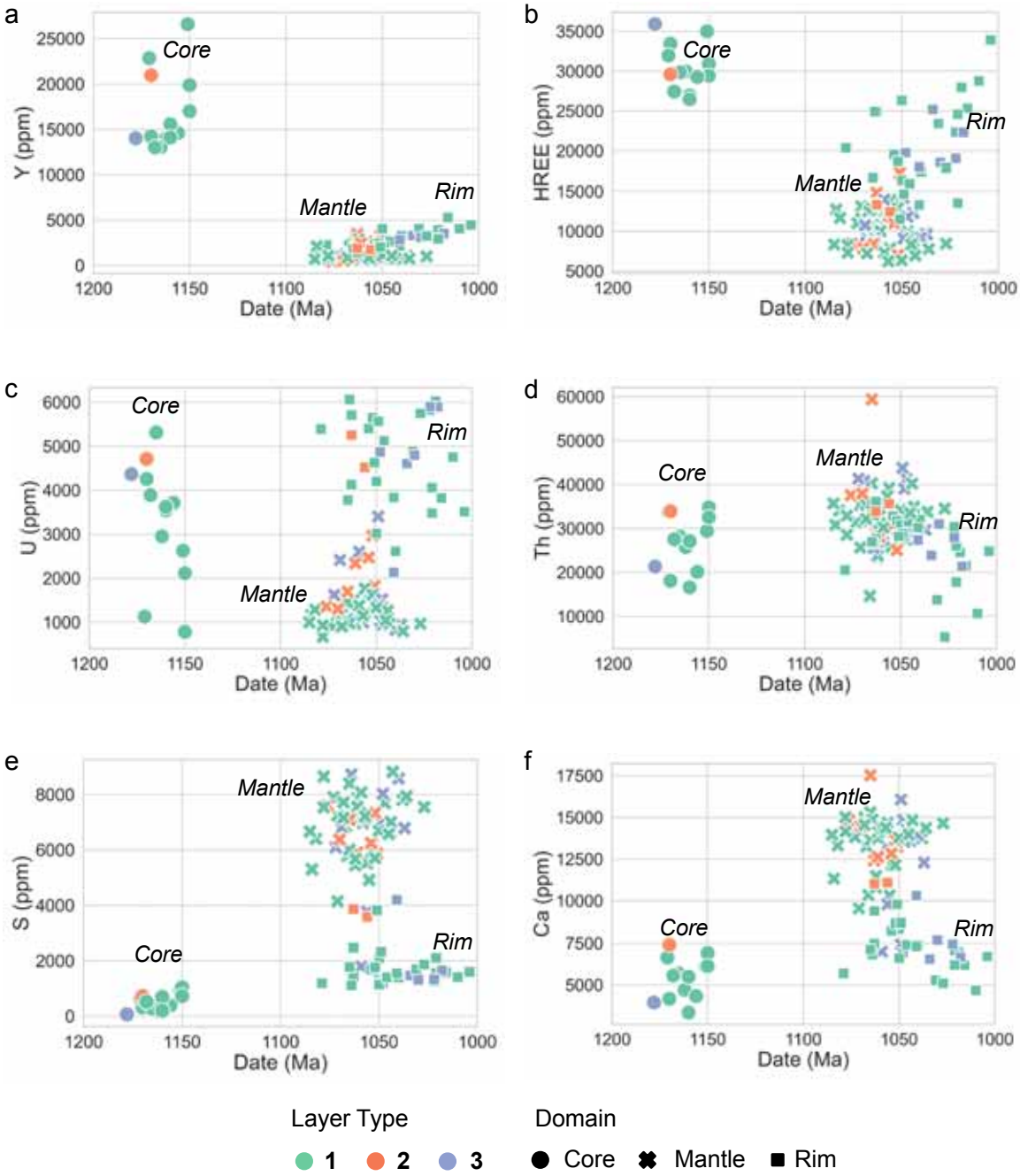

1051

This is the peer-reviewed, final accepted version for American Mineralogist, published by the Mineralogical Society of America.
The published version is subject to change. Cite as Authors (Year) Title. American Mineralogist, in press.
DOI: https://doi.org/10.2138/am-2022-8679. http://www.minsocam.org/

Fig. 9

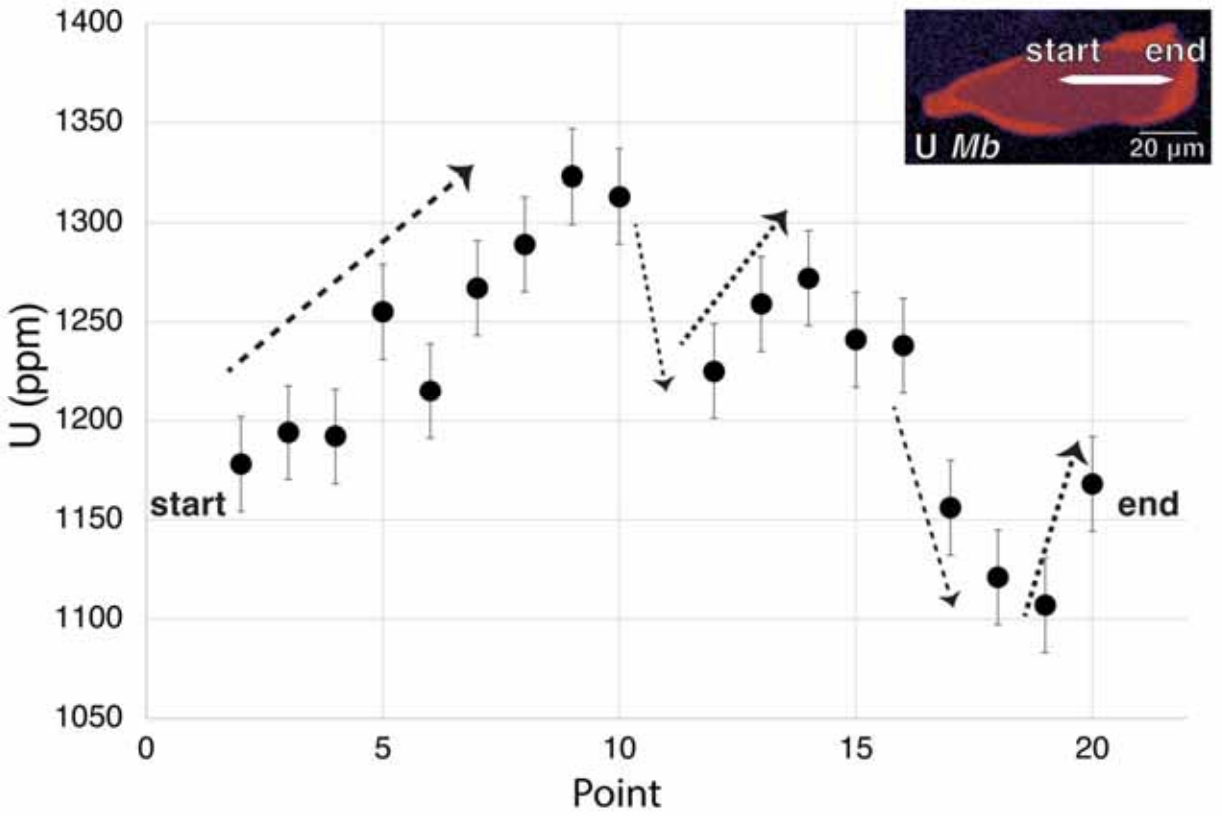

1052

This is the peer-reviewed, final accepted version for American Mineralogist, published by the Mineralogical Society of America.
The published version is subject to change. Cite as Authors (Year) Title. American Mineralogist, in press.
DOI: https://doi.org/10.2138/am-2022-8679. http://www.minsocam.org/

Fig. 10

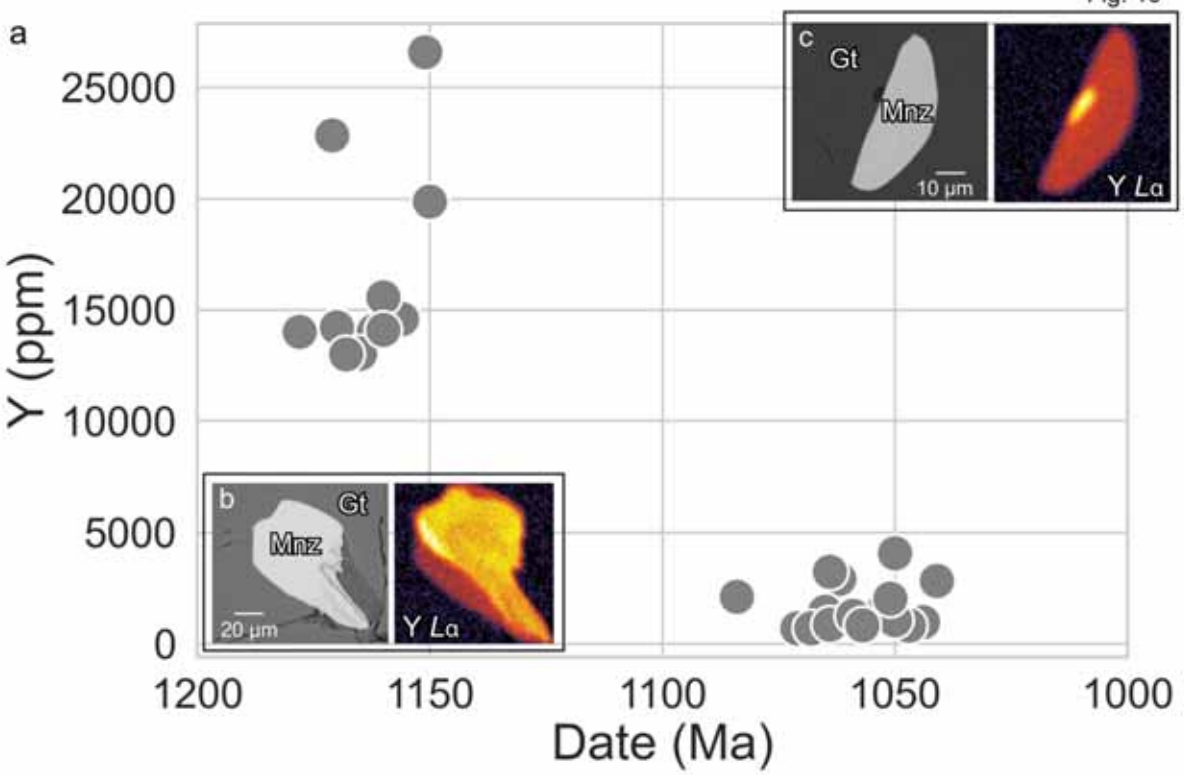

1053

This is the peer-reviewed, final accepted version for American Mineralogist, published by the Mineralogical Society of America.
The published version is subject to change. Cite as Authors (Year) Title. American Mineralogist, in press.
DOI: https://doi.org/10.2138/am-2022-8679. http://www.minsocam.org/

Fig. 11

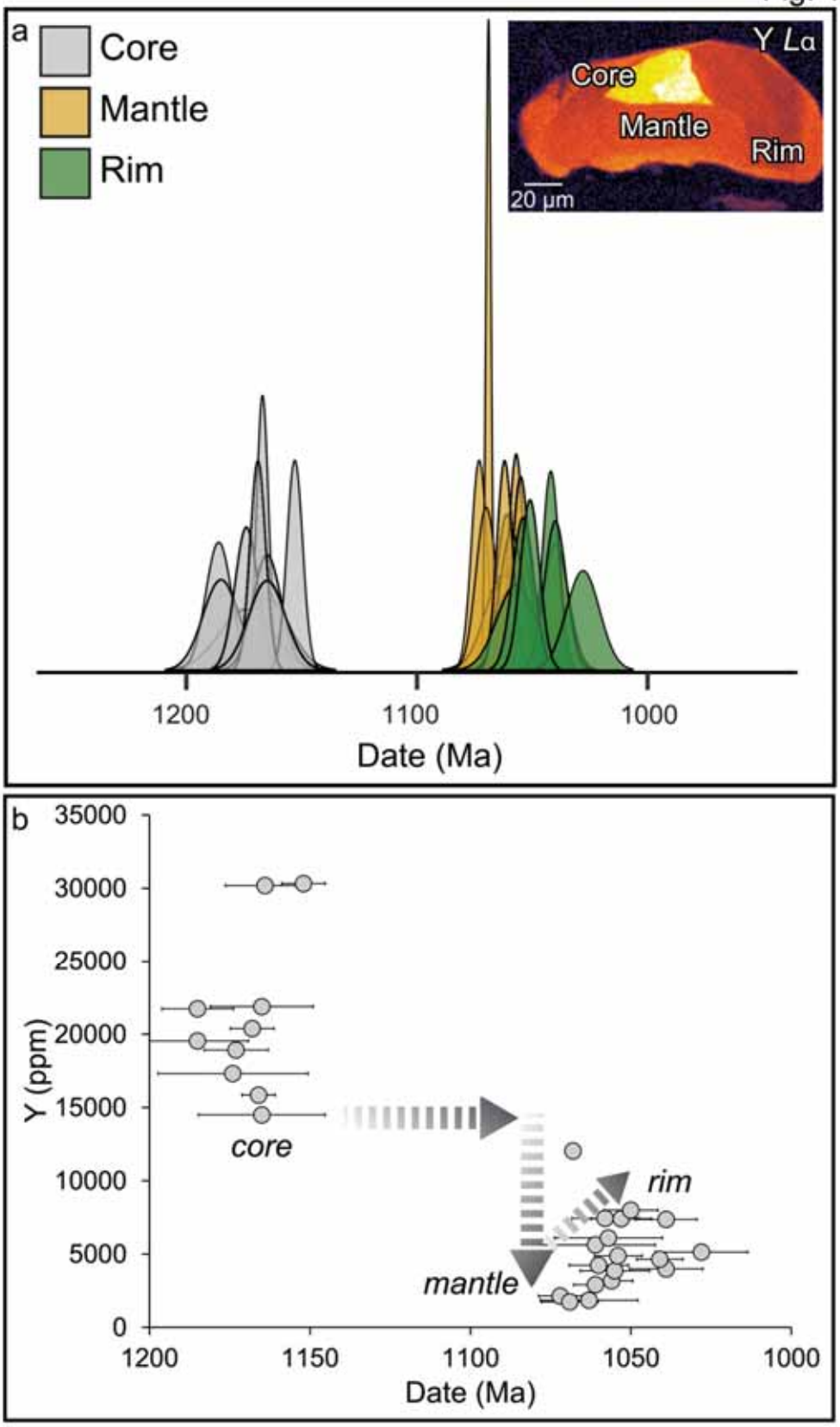

1054

This is the peer-reviewed, final accepted version for American Mineralogist, published by the Mineralogical Society of America.
The published version is subject to change. Cite as Authors (Year) Title. American Mineralogist, in press.
DOI: https://doi.org/10.2138/am-2022-8679. http://www.minsocam.org/

Fig. 12

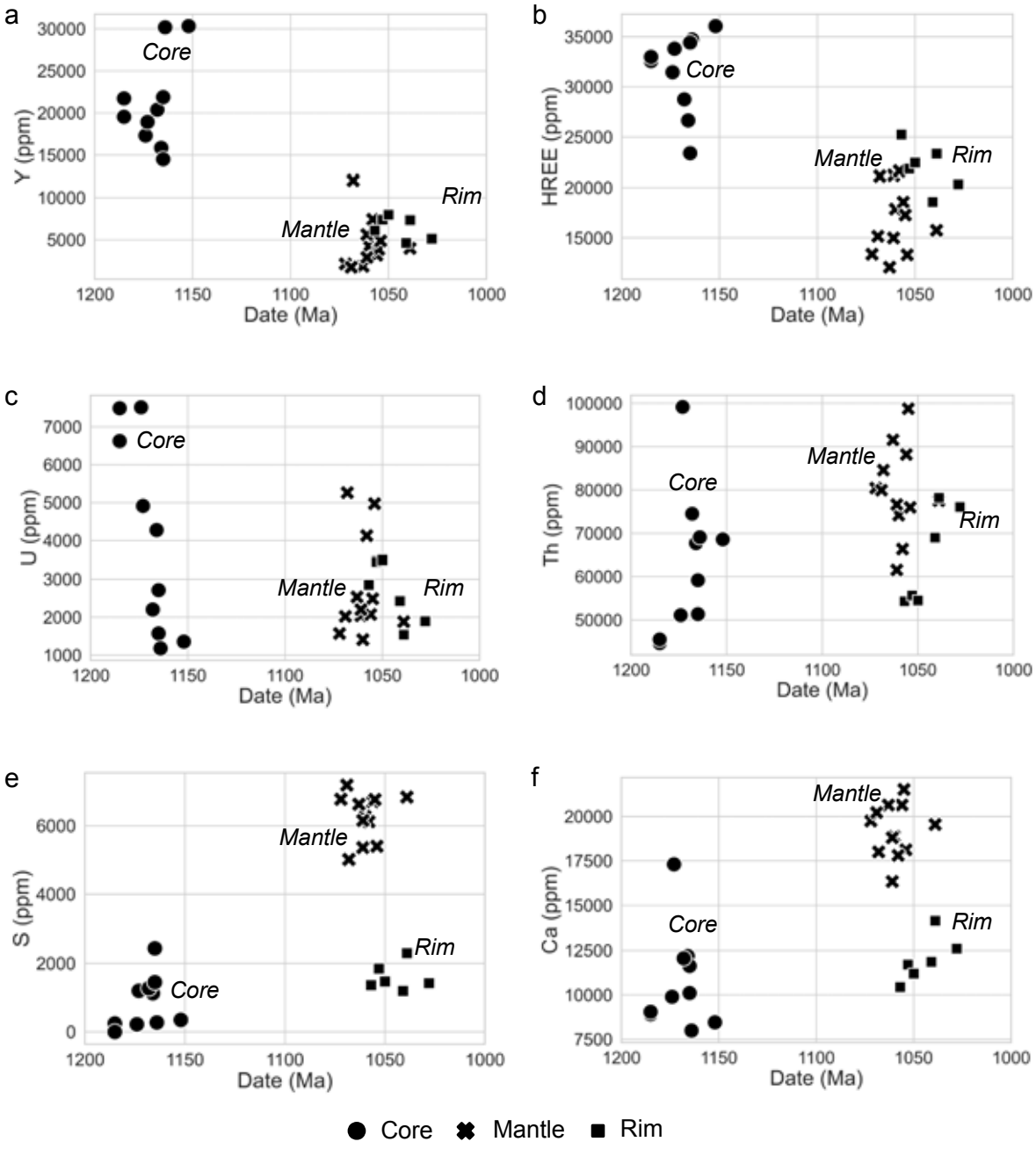

1055

Fig. 13

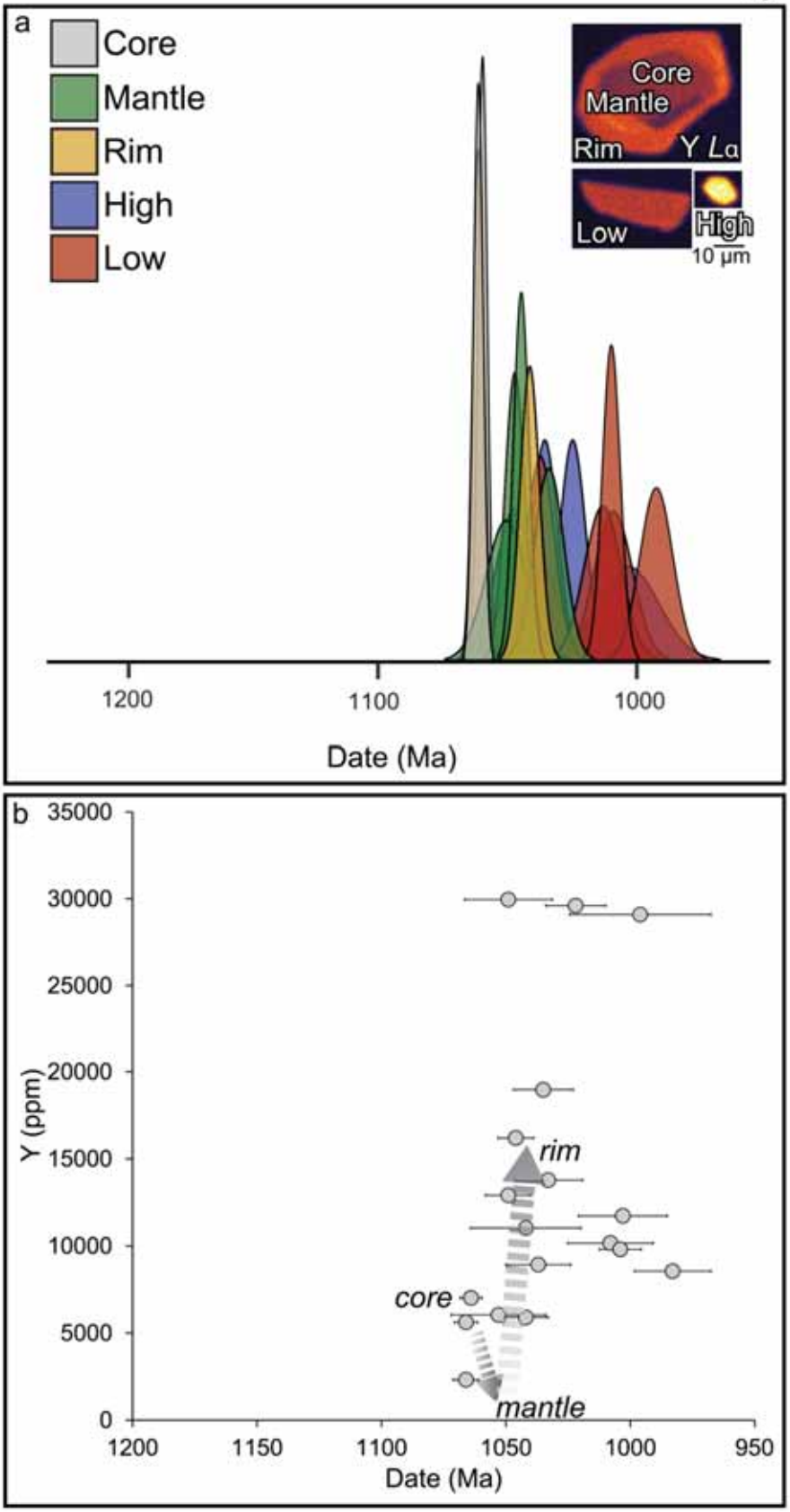

1056

This is the peer-reviewed, final accepted version for American Mineralogist, published by the Mineralogical Society of America.
The published version is subject to change. Cite as Authors (Year) Title. American Mineralogist, in press.
DOI: https://doi.org/10.2138/am-2022-8679. http://www.minsocam.org/

Fig .14

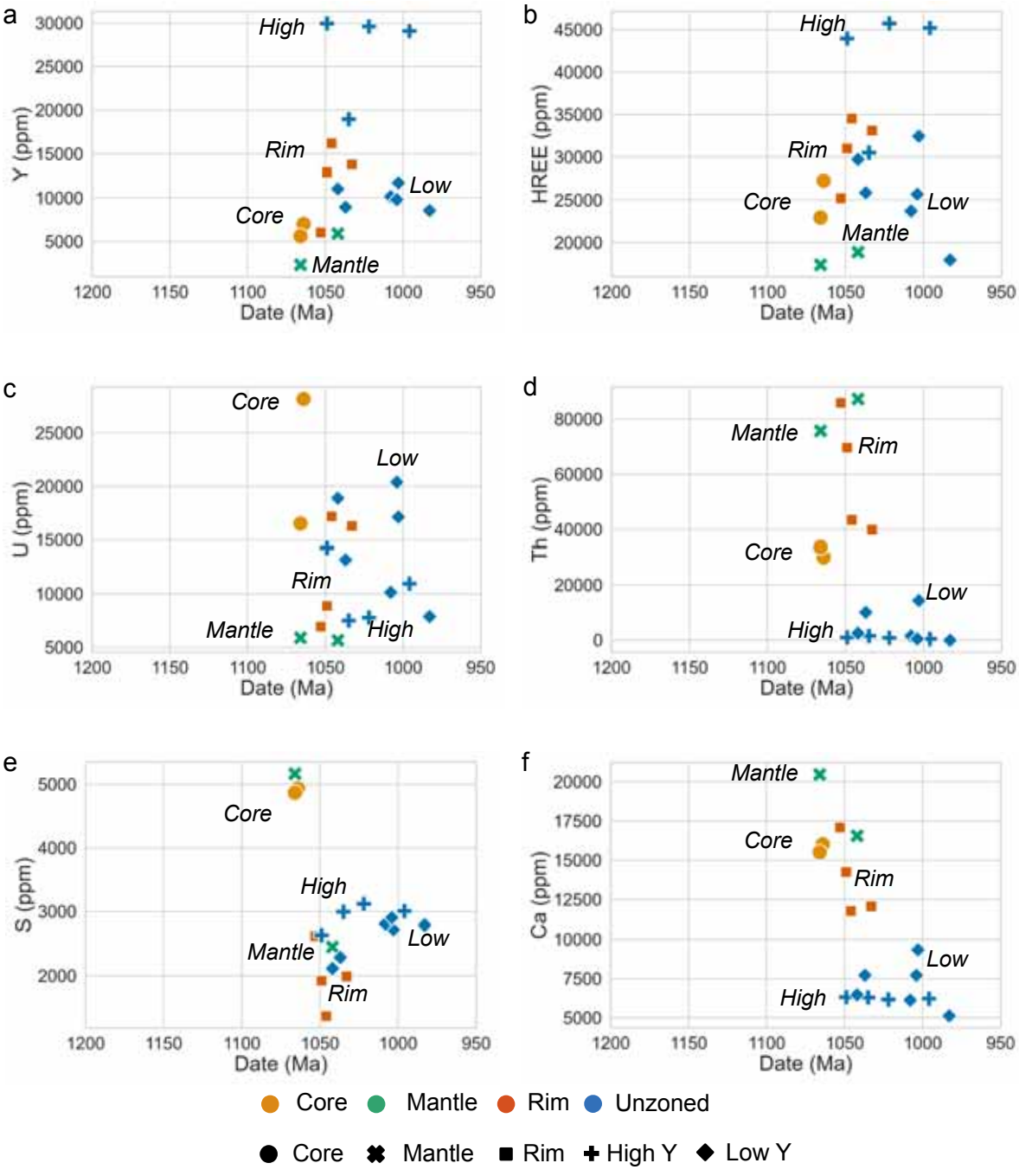

1057

This is the peer-reviewed, final accepted version for American Mineralogist, published by the Mineralogical Society of America.
The published version is subject to change. Cite as Authors (Year) Title. American Mineralogist, in press.
DOI: https://doi.org/10.2138/am-2022-8679. http://www.minsocam.org/

Fig. 15

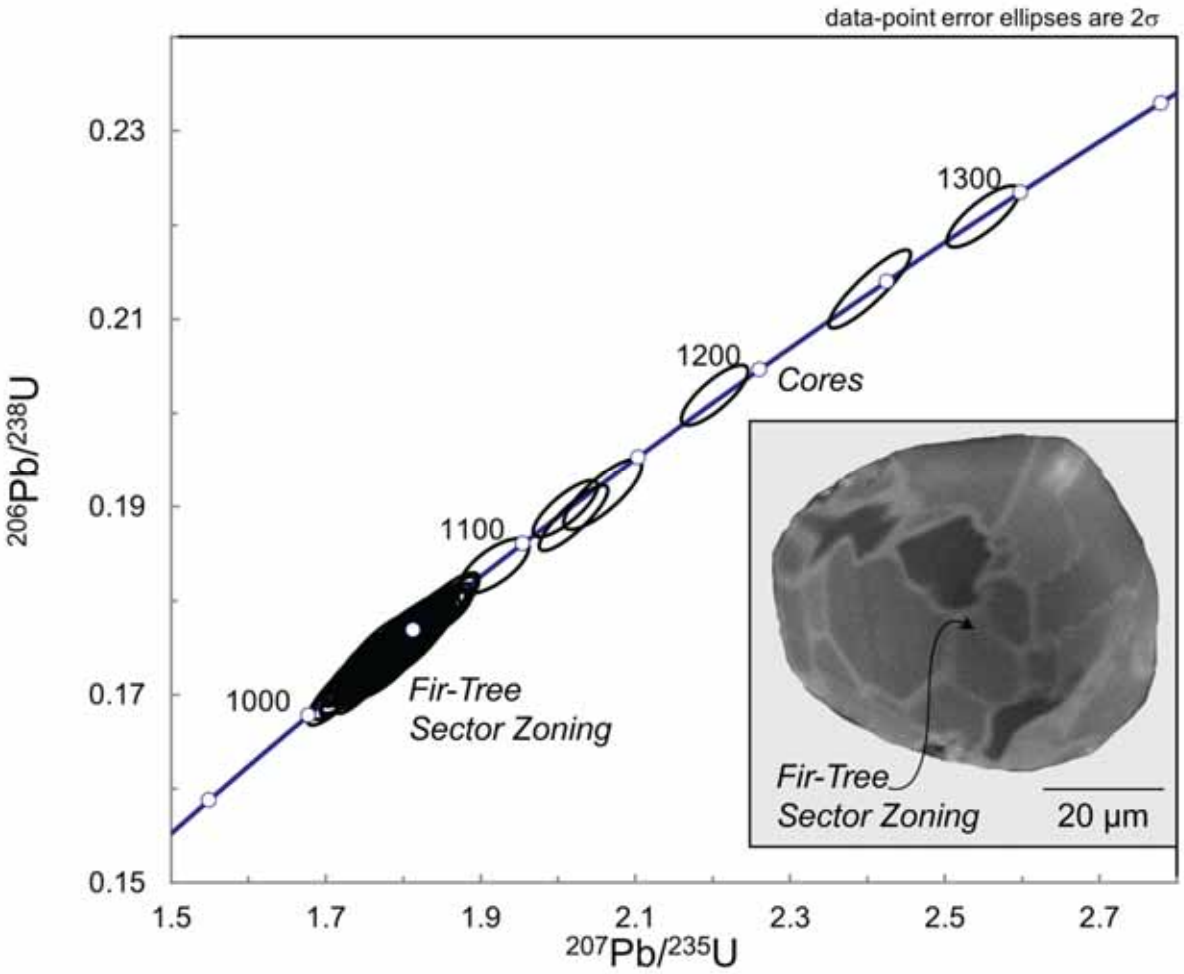

1058

This is the peer-reviewed, final accepted version for American Mineralogist, published by the Mineralogical Society of America.
The published version is subject to change. Cite as Authors (Year) Title. American Mineralogist, in press.
DOI: https://doi.org/10.2138/am-2022-8679. http://www.minsocam.org/

Fig. 16

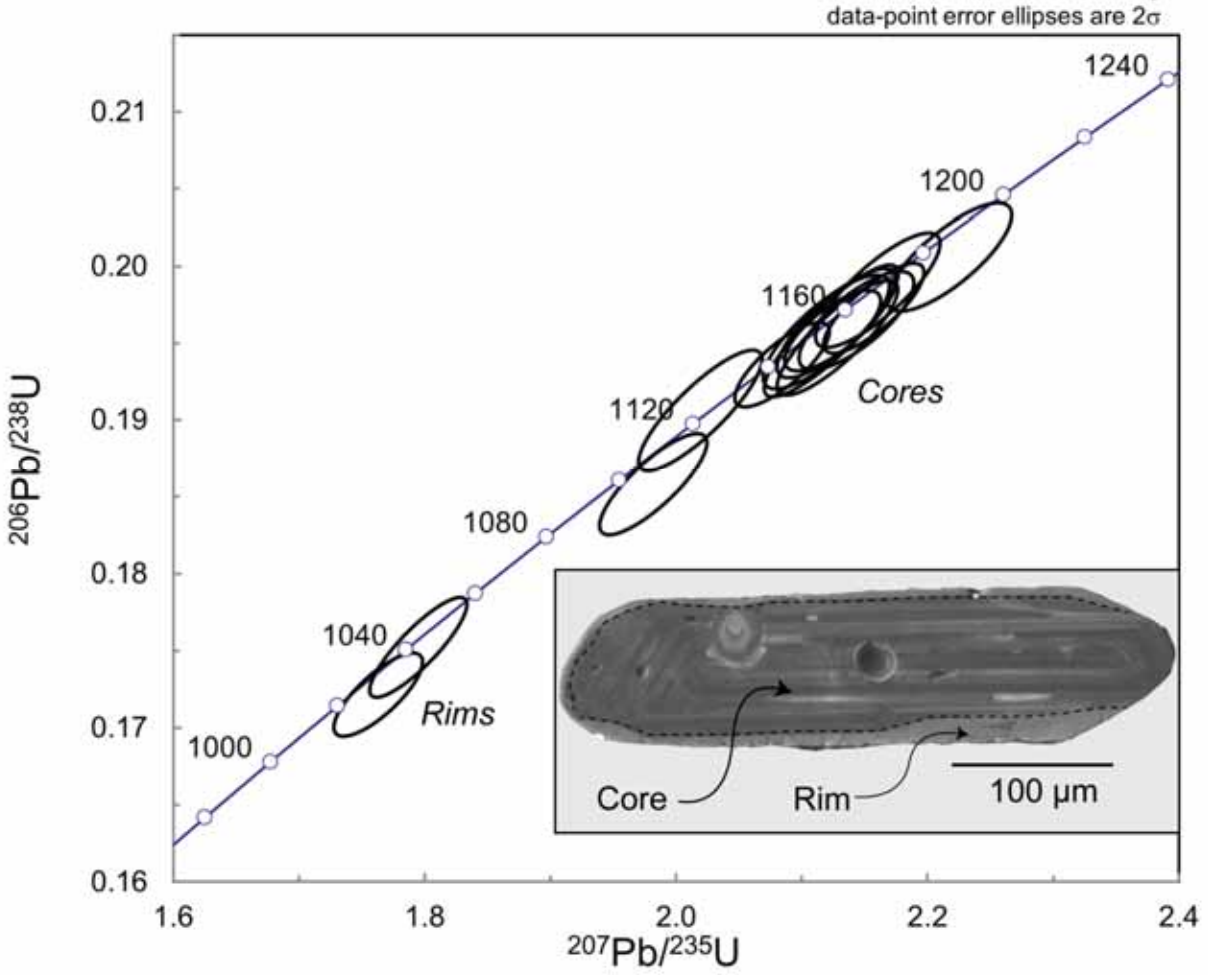

1059

This is the peer-reviewed, final accepted version for American Mineralogist, published by the Mineralogical Society of America.
The published version is subject to change. Cite as Authors (Year) Title. American Mineralogist, in press.
DOI: https://doi.org/10.2138/am-2022-8679. http://www.minsocam.org/

Fig. 17

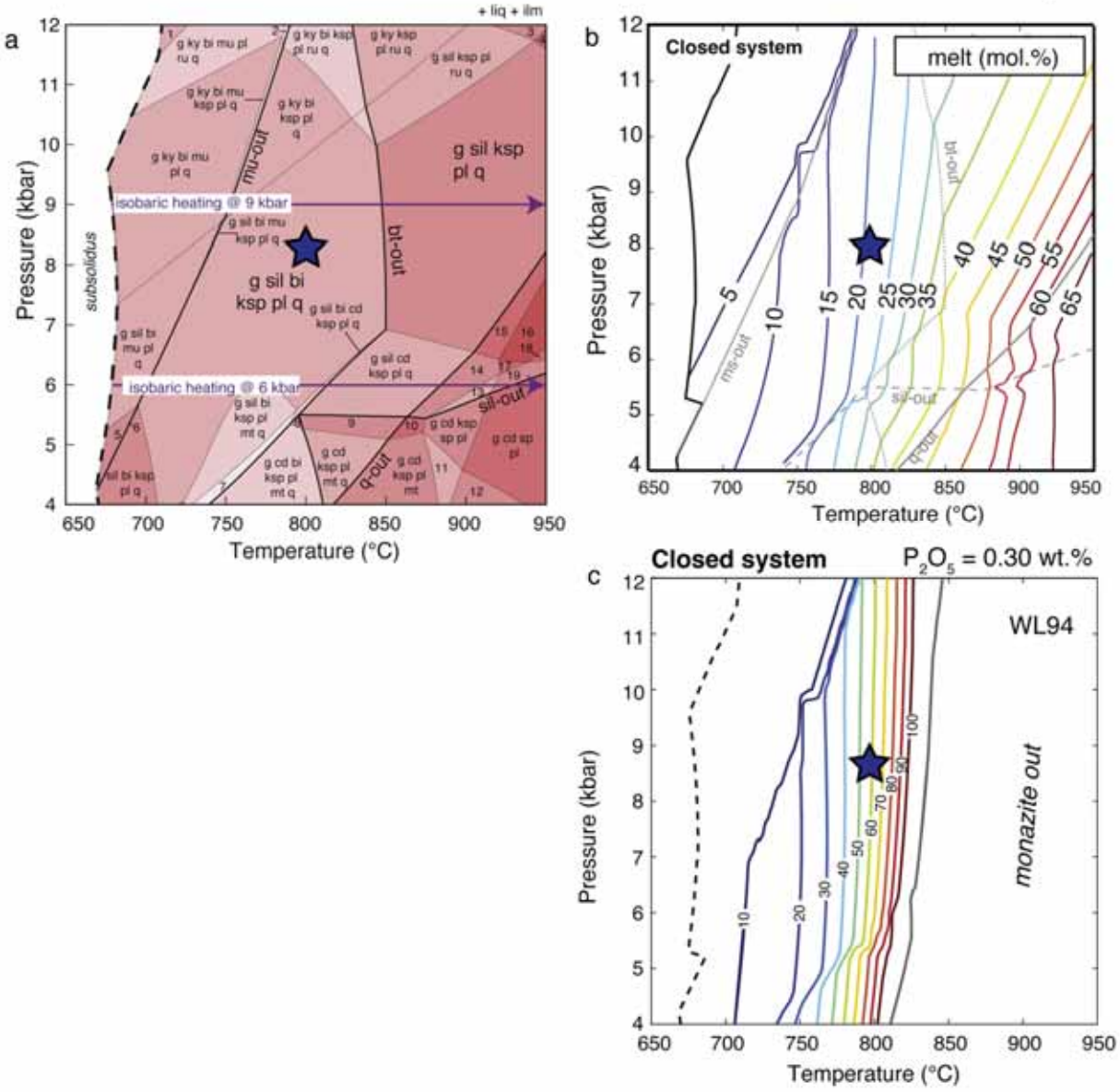

1060

This is the peer-reviewed, final accepted version for American Mineralogist, published by the Mineralogical Society of America.
The published version is subject to change. Cite as Authors (Year) Title. American Mineralogist, in press.
DOI: https://doi.org/10.2138/am-2022-8679. http://www.minsocam.org/

Fig. 18

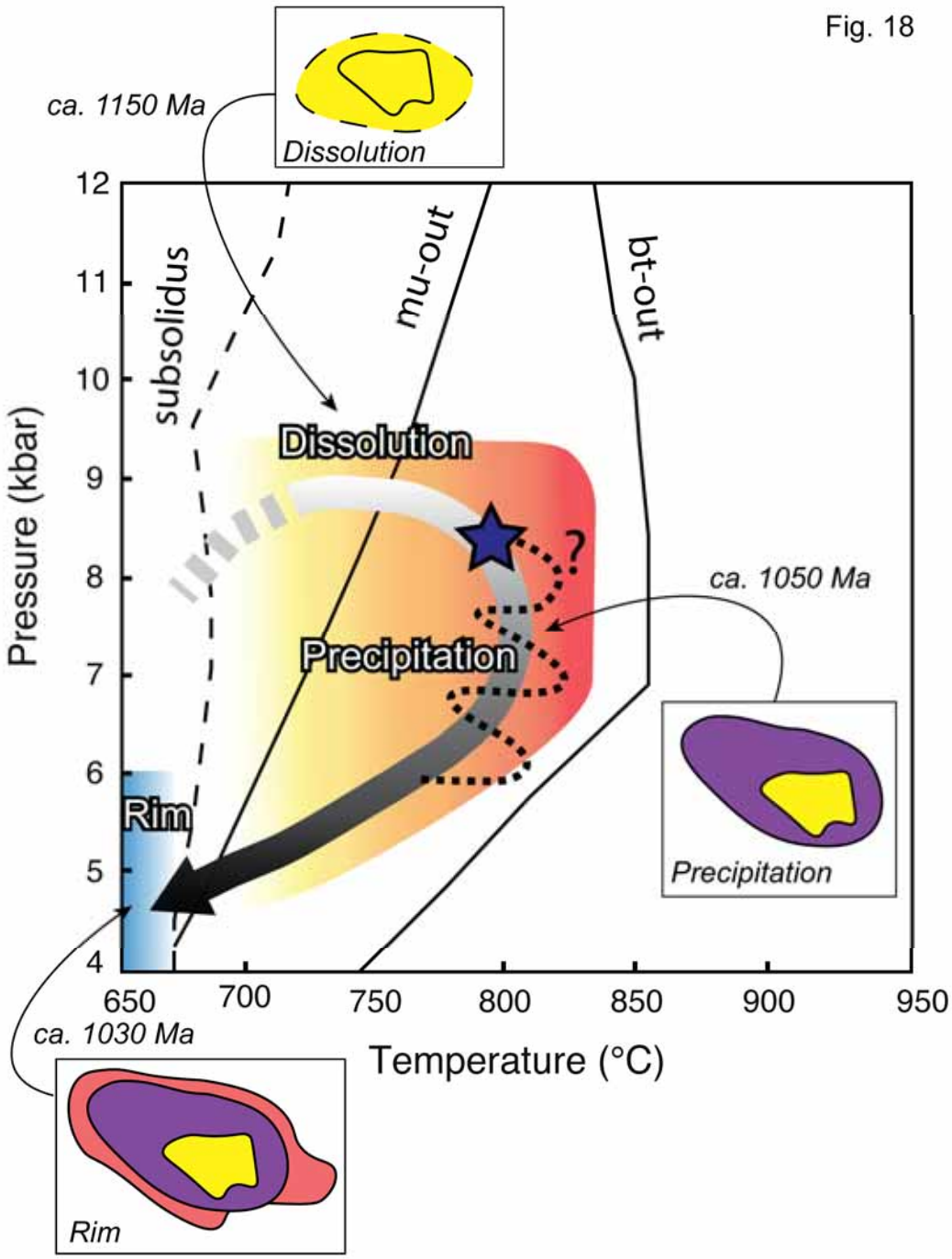

1061

This is the peer-reviewed, final accepted version for American Mineralogist, published by the Mineralogical Society of America.
The published version is subject to change. Cite as Authors (Year) Title. American Mineralogist, in press.
DOI: https://doi.org/10.2138/am-2022-8679. http://www.minsocam.org/

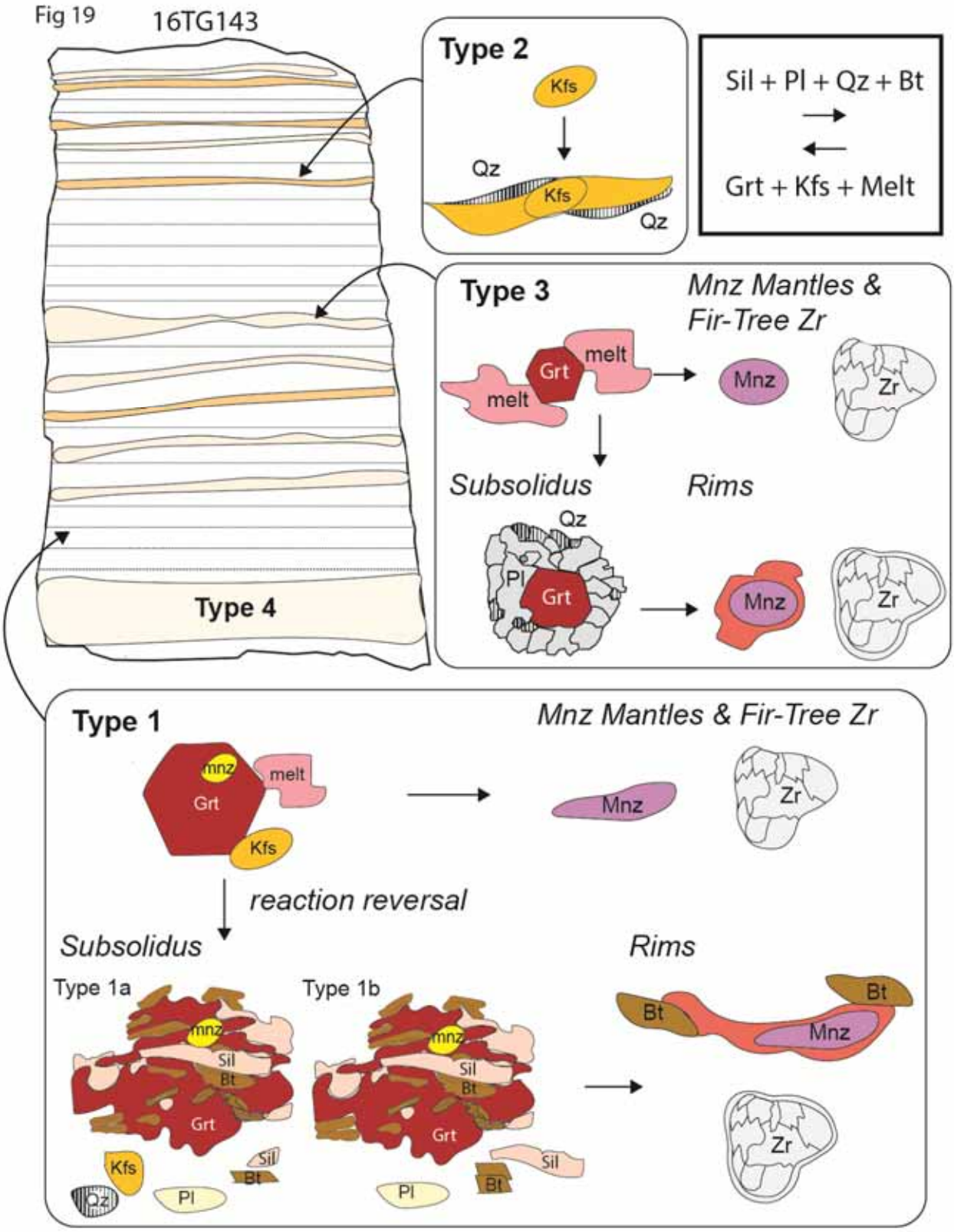

1062

This is the peer-reviewed, final accepted version for American Mineralogist, published by the Mineralogical Society of America.
The published version is subject to change. Cite as Authors (Year) Title. American Mineralogist, in press.
DOI: https://doi.org/10.2138/am-2022-8679. http://www.minsocam.org/

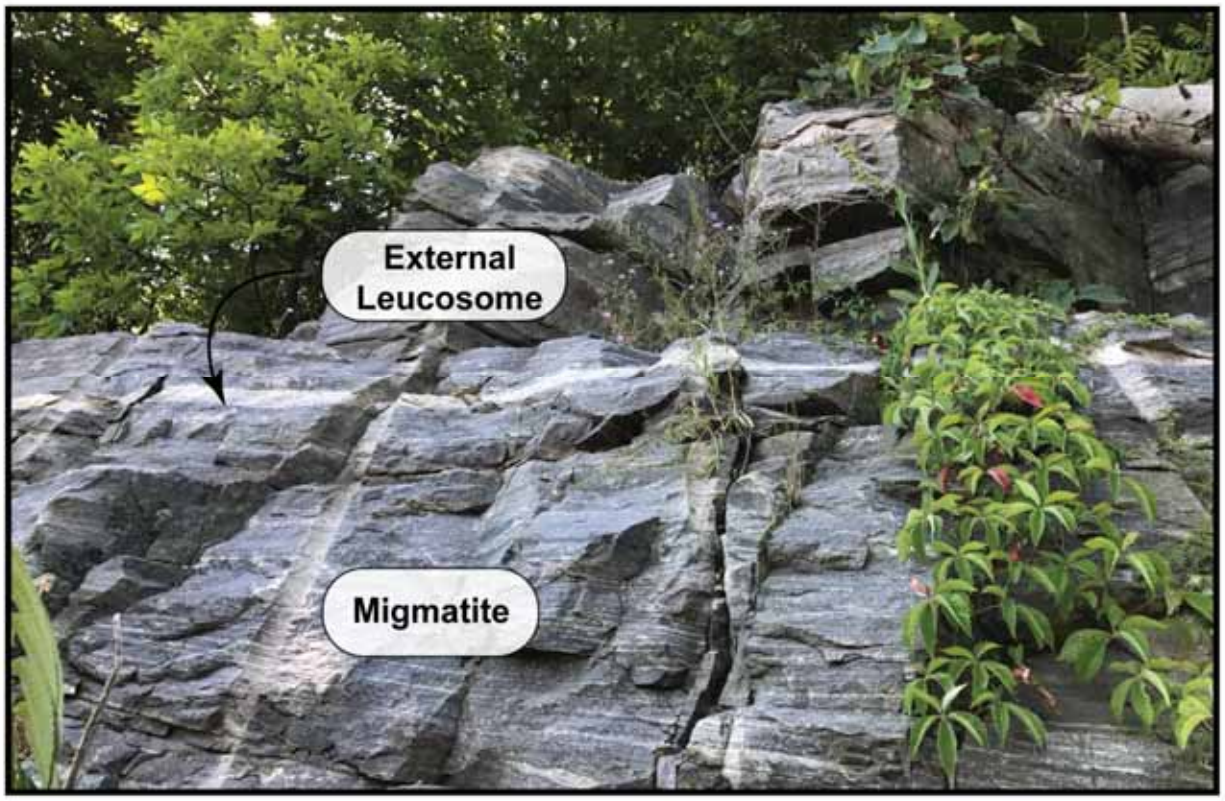

1063